Monolithic Superconducting Emitter of Tunable Circularly Polarized Terahertz Radiation

A. Elarabi,[1,2,*] Y. Yoshioka,[1] M. Tsujimoto,[1,2] and I. Kakeya[1,†]

[1]*Department of Electronic Science and Engineering, Kyoto University, Nishikyo, Kyoto 615-8510, Japan*
[2]*Faculty of Pure and Applied Sciences, University of Tsukuba, 1-1-1 Ten-nodai, Tsukuba, Ibaraki 305-8573, Japan*

(Received 24 August 2017; revised manuscript received 15 November 2017; published 29 December 2017)

We propose an approach to controlling the polarization of terahertz (THz) radiation from intrinsic Josephson-junction stacks in a single crystalline high-temperature superconductor $Bi_2Sr_2CaCu_2O_8$. Monolithic control of the surface high-frequency current distributions in the truncated square mesa structure allows us to modulate the polarization of the emitted terahertz wave as a result of two orthogonal fundamental modes excited inside the mesa. Highly polarized circular terahertz waves with a degree of circular polarization of more than 99% can be generated using an electrically controlled method. The intuitive results obtained from the numerical simulation based on the conventional antenna theory are consistent with the observed emission characteristics.

DOI: 10.1103/PhysRevApplied.8.064034

I. INTRODUCTION

The terahertz frequency range (0.3–10 THz) has attracted a considerable amount of interest in recent years. This is largely because of the numerous vibrational and rotational molecular absorption lines it contains which are used as marking regions in spectroscopy applications [1]. Ever since the demonstration of an intense terahertz radiation from a stack of intrinsic Josephson junctions (IJJs) made from $Bi_2Sr_2CaCu_2O_{8+\delta}$ (Bi-2212) [2], there has been an increased interest in the development of IJJ-based devices as highly promising emitters of coherent continuous-wave terahertz radiations [3–5]. Imaging, sensing, and spectroscopy applications require some control over the properties of radiations emitted from terahertz sources. The polarization of terahertz radiations is of special importance in vibrational circular dichroism spectroscopy [6,7], high-speed telecommunications, and terahertz continuous-wave polarization imaging [8]. In laboratory setups, circular polarization (CP) can be realized through use of optical devices, such as quarter-wave plates; however, the use of compact monolithic sources has proven to be less costly and more suitable for applications that require portability. Circularly polarized terahertz emissions have recently been experimentally achieved by utilizing monolithic devices, such as quantum cascade lasers [9,10] and resonant-tunneling diodes [11]. Compared to these devices, IJJ-based sources can cover wider frequency ranges, which are unattainable by other terahertz sources [4]. Furthermore, the emission intensity of IJJ-based devices can also be thermally controlled, both internally [12,13] and externally [14,15]. By applying a direct current (dc) voltage (V_b) across the c axis of IJJs stacked in a mesa form, a high-frequency (HF) current is generated along with emission of subterahertz radiation at the Josephson frequency given by $f_J = (2eV_b/hN)$, where h, e, and N denote the Planck constant, elementary charge, and number of contributing IJJs, respectively. The emission of high-intensity radiation is observed when the oscillating IJJs resonate in the excited cavity mode [2,3]. Extant studies have investigated the excited cavity modes in Bi-2212 mesa structures by observing the distribution of the far-field intensity as a function of the azimuth angle [16,17]. Additionally, the patch antenna model [18,19] has been found useful in describing the coupling between space and Josephson plasma waves inside the mesa structure [20–24]. A more direct approach to determine the excited cavity mode is to measure the polarization of the emitted radiation as a function of the mesa shape and bias conditions. These factors have, thus far, remained uninvestigated.

Waves emitted from rectangular IJJ-based sources have been known to be linearly polarized [2]. However, recent numerical studies [14,25,26] have proposed the possibility of realizing circularly polarized emissions from IJJ devices. This paper reports the experimental demonstration of the generation of circularly polarized subterahertz waves from a monolithic source—a superconducting IJJ stack—wherein the ellipticity and evolution direction are tuned by mesa shape and bias conditions. The highest degree of circular polarization (DOCP) recorded in the study proposed herein is 99.7%, which is higher than that recorded by state-of-the-art quantum cascade lasers used for obtaining circular polarization [9,10,27]. As circularly polarized terahertz waves could be employed in a wide variety of potential applications, the result obtained in this

*Corresponding author.
asemelarabi@sk.kuee.kyoto-u.ac.jp
†Corresponding author.
kakeya@kuee.kyoto-u.ac.jp

study, along with recently reported packaging [28] and the demonstration of the terahertz torch [29], it is believed, will significantly influence and inspire the development of practical applications of IJJ-based terahertz emission devices [4,30].

II. EXPERIMENTAL METHOD

A. Samples design and fabrication

The mesa-shaped design is based on the truncated-edge square microstrip patch antenna [18,31–33]. Figures 1(a) and 1(b), respectively, depict a schematic of the IJJ-based device developed in this study and a microscopic image of sample 2. The mesa structure is fabricated from a Bi-2212 single crystal using photolithography and Ar-ion milling [13]. Circular polarization in the proposed design is realized through the excitation of two transverse orthogonal modes along the major and minor diagonals, as depicted in Figs. 1(d) and Video 1. On account of the small area of the truncated edge, the two above-mentioned transverse modes exhibit adjacent resonant frequencies. The mesa shape is designed with a perturbation to mix the two modes at the cavity resonant frequency (i.e., the arithmetic mean of the two adjacent resonant frequencies) with a phase difference of $\pi/2$ radians between them thereby forming a rotating surface current (refer to the animation in Video 1). According to the antenna theory, electric fields corresponding to the two above-mentioned eigenmodes could be mathematically represented by $E_1 = (\sqrt{S}/w)(\sin kx - \sin ky)$ and $E_2 = (\sqrt{S}/w)(\sin kx + \sin ky)$ [31,32], where w is the total length of the square side and $k = \pi/w$. The most significant design parameters that control the polarization state of the emitted radiation comprise the untruncated surface area S, the trimmed surface area Δs (perturbation), and the feeding electrode position, as depicted in Fig. 1(d). The resonant frequencies of these two modes are given by $f_1 = f_{0r}$ and $f_2 = f_{0r}(1 + 2\Delta s/S)$ with $f_{0r} = c_0/2nw$ [18,32,34], where c_0 is the speed of light in vacuum and n is the refractive index. The electric field distribution of the mixed mode can be represented by the linear combination of the two above-mentioned modes, as given below.

$$E_z = E_1 e^{i2\pi f_1 t} + E_2 e^{i(2\pi f_2 t + \delta)}, \quad (1)$$

where δ is the phase difference between the two modes. The above equation demonstrates that the first mode is antisymmetric with respect to the minor diagonal axis, and the second mode is antisymmetric with respect to the major diagonal axis, as depicted in Fig. 1(d). Therefore, the critical current density distribution j_c must be antisymmetric with respect to both axes for the two modes to be excited at the same time. This implies that the feeding point must be on either the x or y axis for circular polarization to be achieved [35].

As oscillations in the proposed device are generated locally by Josephson junctions, the local rise in mesa temperature due to dc current injection acts as a perturbation to address the degeneracy of the two CP modes [36]. Antenna theory predicts that the position of an electrode, feeding HF from the source, with respect to the truncated

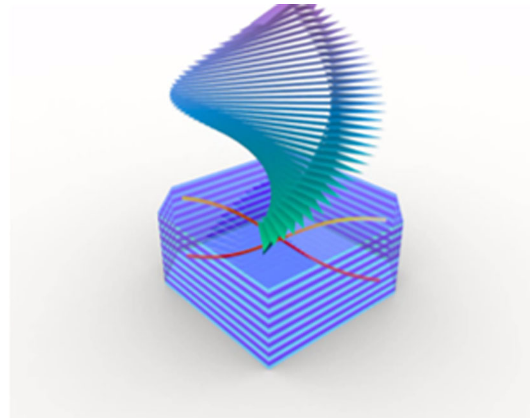

VIDEO 1. Electric-field distribution and circularly polarized radiation propagation and direction.

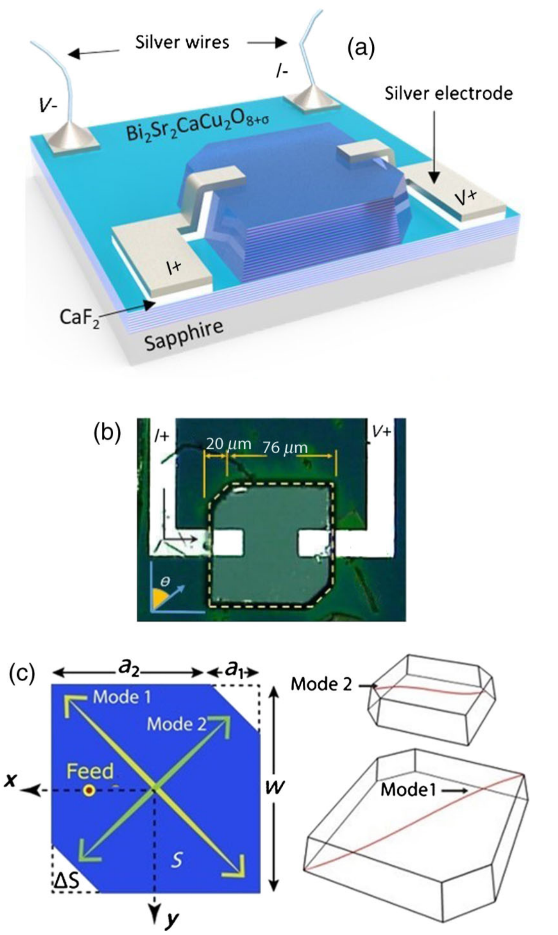

FIG. 1. (a) Schematic of Bi-2212 terahertz emitter. (b) Optical microscopic image of sample 2. (c) Excitation of the two orthogonal transverse modes along the major and minor diagonals in the x-y plane.

edges determines the direction of rotation of the emissions [left-hand *CP* (LHCP) or right-hand *CP* (RHCP)] [18,37]. This implies that when the truncated edge is on the left side of the feeding point, RHCP emission is obtained and vice versa. Nonetheless, as mentioned earlier, the high-frequency feeding in the device under study is generated inside the mesa structure on account of dc current injection. This might altogether result in a rotational direction that may be different from the ones described above; this has been discussed later in this paper.

B. Electromagnetic simulation

The initial design parameters are determined using the commercial full-wave three-dimensional finite-element electromagnetic simulation software—Ansys HFSS [26]. Similar simplified methods have previously been used to determine cavity resonance conditions [26,38], and a more advanced method, capable of solving sine-Gordon equations, is used to determine polarization properties [25]. A model similar to that reported in Ref. [26] is used, wherein the dielectric constant $\epsilon = 17.6$, and the feeding point is placed over the horizontal axis of the geometry. To account for the losses incurred owing to the skin effect, an impedance boundary condition is applied to the model [39], and the complex surface impedance is estimated by using both the Zimmermann method [26,39,40] and the *a*-*b* surface resistance correction [41] given by $R_s = \frac{1}{2}\mu_0^2\sigma'\omega^2\lambda^3$, where $\sigma' = 2/\omega\mu\delta_s^2$, δ_s is the skin depth, ω is the angular frequency, μ is the magnetic permeability, and $\lambda = 210$ nm is the penetration depth.

Figure 2(b) depicts a comparison of the axial ratios (ARs) determined through simulation of the proposed model and experimental results obtained from sample 3. The proposed model had parametric dimensions comparable to those of sample 3. Dimensions of the proposed model are $a_1 = 13\ \mu$m and $a_2 = 69\ \mu$m, where a_1 and a_2 represent the side length of the isosceles right-angled triangle-shaped truncated corner of the square microstrip and length of the remainder of the truncated square side, respectively, as shown in Fig. 1(c). The scattering parameter (S_{11}), as determined from the electromagnetic simulation, is shown on the right axis as a green line and demonstrates sharp minima at the two resonant frequencies f_1 and f_2.

C. Measurement setup and polarization characterization

Samples are mounted on a Cu cold finger placed inside a He-flow cryostat with a transparent optical window, as depicted in Fig. 2(a). The radiation characteristics are detected by using a Si bolometer and lock-in amplifier. The polarization is then measured by rotating a wire-grid polarizer in the beam path and recording the angle-dependent intensity. To characterize the polarization of the emissions, the polarization ellipse [10,42] is obtained by using the detected intensity as a function of the polarizer angle. The polarization state is best represented by the axial ratio for the entire emission range. The axial ratio, in dB, is defined as the ratio of the lengths of the major and minor axes (maximum and minimum intensities) of the polarization ellipse fitted to the polar plot of the detected intensity as a function of the polarizer angle; i.e., $\mathrm{AR} = 20[\log[I_{\max}/I_{\min}]]$. It is to be noted that polarization with an AR of less than 3 dB can be regarded as *CP* [37]. Frequency measurements are performed using a high-resolution lab-built Martin-Puplett FTIR interferometer [43], wherein the estimated emission frequency is obtained through linear interpolation of the measured data.

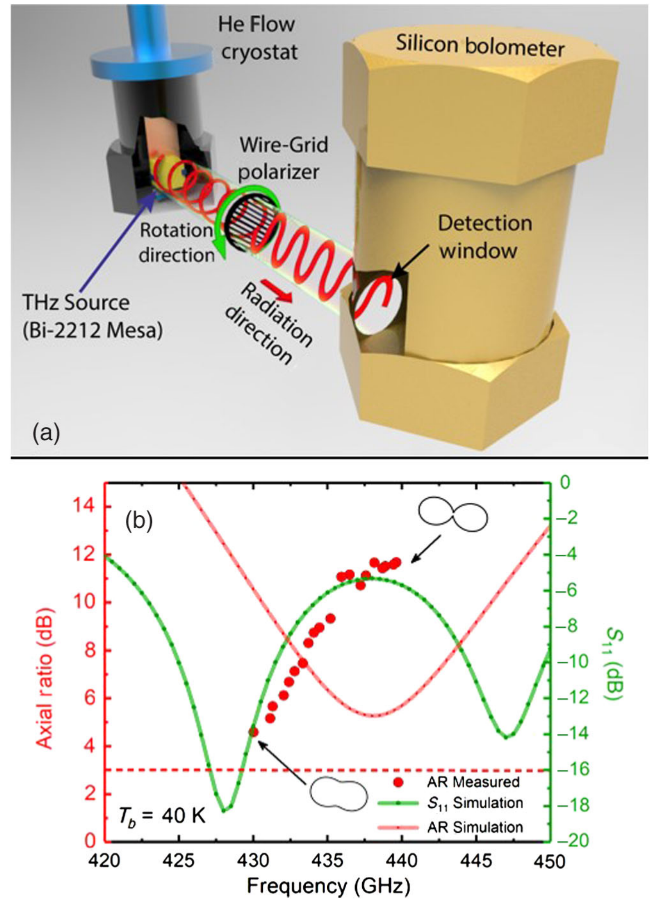

FIG. 2. (a) Schematic of the experimental setup for polarization characterization. (b) Axial ratio comparison between sample 3 and the results obtained from electromagnetic simulation.

III. RESULTS AND DISCUSSIONS

To discuss the effect of design parameters on the polarization state, we present the emission features of three samples with different a_2/a_1 values. The values of a_1 and a_2 and the thickness t of the mesa structure for the three samples are summarized in Table I. *I*-*V* characteristics (IVC) and device emissions (precharacterization) are first confirmed followed by polarization measurement through use of the above-mentioned setup [Fig. 2(a)].

TABLE I. Design and experimental parameters as well as radiation properties of the three samples used in this study.

	Sample	1	2	3
Design parameters (μm)	a_1	16	20	13
	a_2	70	76	69
	w	86	96	82
	a_2/a_1	4.38	3.8	5.3
	t	2.25	1.9	2.4
Temperatures (K)	T_b	21	22	40
	T_c	84	83.3	82
Radiation properties	P_{max} (nW)	176.5	23.5	123.5
	$\mathrm{AR}_{\mathrm{min}}$ (dB)	0.2	0.49	4.6
	DOCP (%)	99.7	99	77.8

Sample 1, along with all other samples, exhibits typical characteristics of slightly underdoped Bi-2212 mesas. IVC of sample 1 is depicted in Fig. 3(a) along with its detection intensity measured at the outermost IVC branch. In this study, all polarization measurements as well as IVC determination are performed at the bath temperature corresponding to the highest emission intensity ($T_b = 21$ K). At about 13.4 mA, a sharp voltage dip is observed from 1.63 to 1.40 V, which could arguably be attributed to the formation of hot spots [12,44–47]. Emission is observed at a bias voltage $V_b = 1.6$ V and current $I_b = 10.4$ mA with two peaks—9.8 mA at 1.69 V and 8 mA at 1.89 V—as indicated by red arrows in Fig. 3(a). These peaks, at frequencies of 544.3 and 608.6 GHz, may correspond to the excitation of the two cavity modes [25]. The detected power (P), estimated in accordance with bolometer sensitivity, is found to be of the order of $P_{\mathrm{max}} \approx 176.5$ nW.

In the present study, the highest value of CP with $\mathrm{AR} = 0.2$ is obtained under $I_b = 8$ mA and $V_b = 1.9$ V, as depicted in Fig. 3(b). At this point, DOCP is calculated to be 99.7% (See Supplemental Material for the calculation of DOCP [48].) This is the highest DOCP value recorded to date while using a monolithic terahertz source [9,10].

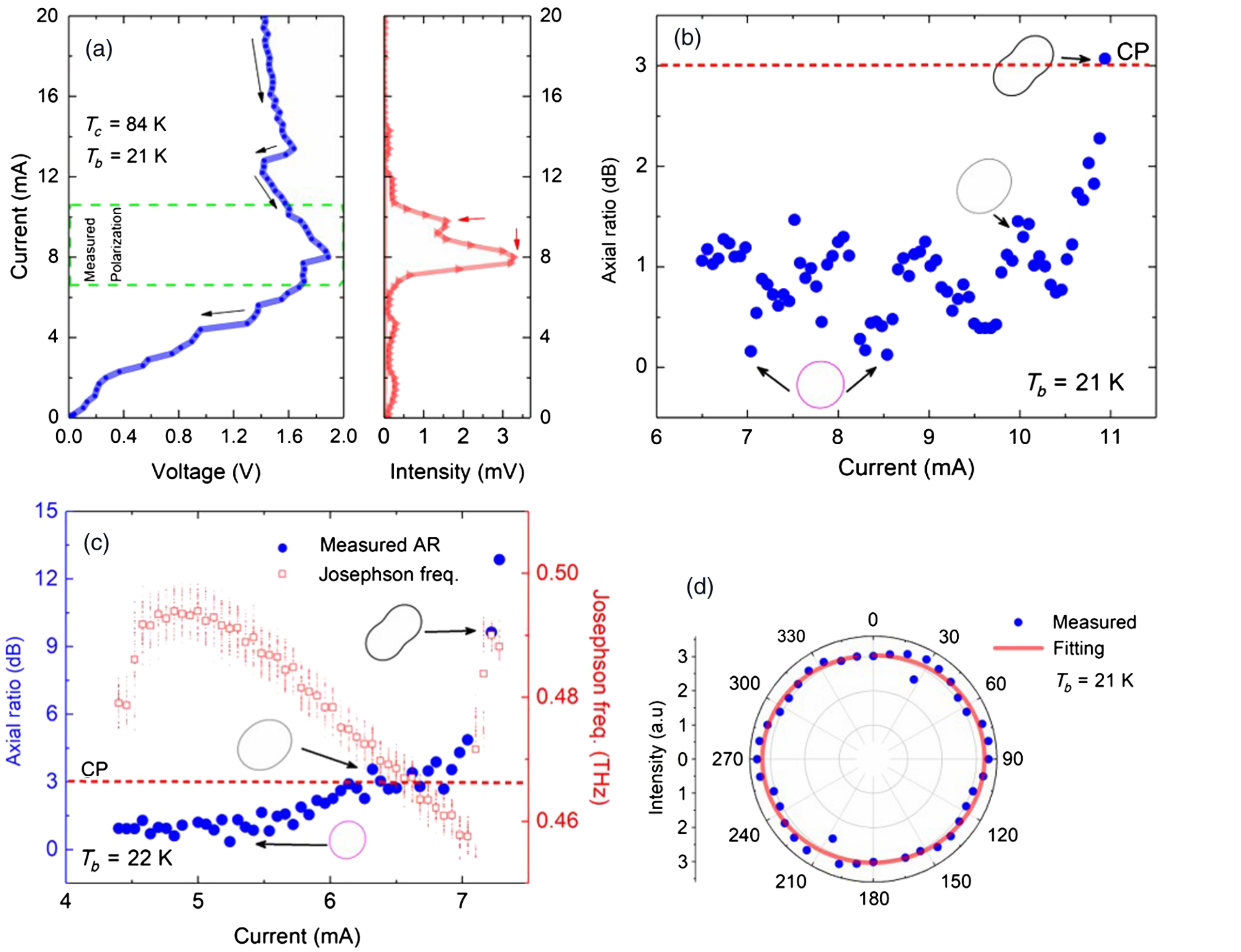

FIG. 3. (a) Return branch of the IVC (left) of sample 1 at $T_b = 21$ K along with the detected emission intensity as a function of bias current (right); AR evolution (blue solid symbols) as a function of the bias current for (b) sample 1; and (c) sample 2; in (c), the red open symbols represent Josephson frequencies estimated from V_b and small dots represent V_b fluctuations during measurements; (d) polar plot of the detected emission intensity as a function of the polarizer angle θ. The data are extracted from Fig. 3(b) at the minimum AR value. The solid lines represent a sinusoidal fitting.

The AR increases accompanying considerable fluctuations as the emission diverges from the optimum bias point. Circularly polarized emission with AR < 3 dB is also observed in sample 2 as seen Fig. 3(c). The lowest AR recorded while using sample 3 is 4.5, which represents an elliptical polarization. Details of the obtained results are summarized in Table I.

The detection of the circularly and elliptically polarized waves is a clear indication of emission attributed to the flow of an in-plane superconducting current on the mesa surface. In a biased Josephson junction, an HF current flows across the barrier at a frequency determined by the ac Josephson relation. A standing wave of half a wavelength is consequently formed with antinodes located at both edges of a Josephson junction. Owing to the synchronization among the excited Josephson junctions in the stack, a net surface current oscillates according to the ac Josephson effect. This current gives rise to an oscillating magnetic field, which couples to surrounding space. In rectangular IJJ mesa devices, whose emissions have been intensively investigated by different groups, the synchronized transverse Josephson plasma wave that causes linearly polarized far-field detection is usually a two-dimensional (2D) standing wave polarized in the direction of the z axis and propagating along the x axis [2,49]. In circularly polarized radiation, the propagation direction of the synchronized transverse Josephson plasma wave rotates at a frequency determined by the ac Josephson relation and resonance frequency relations of the two modes, as shown in Video 1, where f_1 and f_2 in Eq. (1) correspond to Josephson oscillation frequencies.

By directly using the relation between the measured polarization-dependent intensity and the polarization ellipse [10,42], the polarization characteristics of sample 1 are determined. Figure 3(d) captures the polarization-dependent intensity at the minimum AR point in the polar plot. The detected intensity does not depend on θ, although slight deformations in the twofold symmetry may be detected. For samples 2 and 3, minimum AR values obtained in the same manner are 0.5 and 4.5, respectively. The variation in the value of minimum AR with respect to sample geometry is discussed in subsequent paragraphs.

As observed in Fig. 3(b), AR exhibits no significant dependence on bias current and maintains a value less than 1 dB, with a fluctuation of about 0.5 dB, around the minimum AR condition (6.5–10.5 mA). At higher values of I_b (>10.5 mA), the value of AR is seen to rapidly increase. This is a common feature of samples 2 and 3. It may be concluded that when AR > 2 dB, its value is seen to rapidly increase with the deviation of I_b from the optimum bias point. For sample 2, the Josephson frequency estimated by V_b is plotted in Fig. 3(c) along with the current evolution of AR. Any change in V_b results in a corresponding change in the frequency of emission. This effect is believed to be caused by the detection of no signs of variation in the value of N, which usually appears as a discontinuity in measured V_b, during the experiments performed in this study. It is, therefore, considered that the estimated emission frequency varied within the range 0.46–0.50 THz with AR < 3 dB. Results obtained through numerical simulations indicate a steep dip in the minimum value of AR, as depicted in Fig. 4(b) [26]; on the other hand, however, experimental results indicate that AR does not demonstrate a strong dependence on frequency. This discrepancy in the results is believed to be caused by the trapezoidal shape of the mesa. The estimated geometrical resonant frequency exhibited by the geometry at the top of the stack is found to be 13% higher than that exhibited by the geometry at the bottom. This is supposed to be caused by an entrainment effect, wherein synchronization occurs between thousands of stacked IJJs at frequencies determined by the geometry of a part of the stack. Accordingly, the frequency range over which circular polarization is achieved is found to

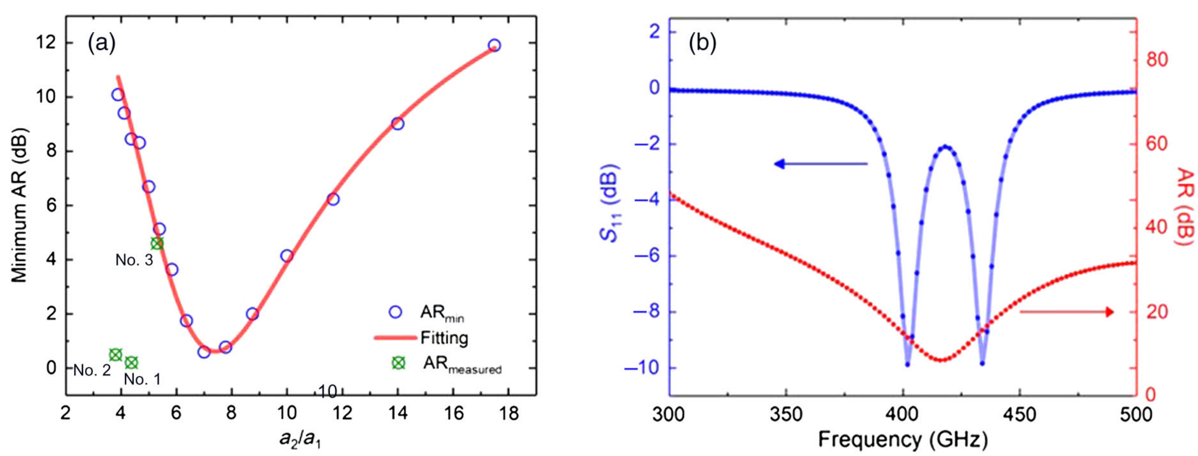

FIG. 4. (a) Minimum values AR vs dimensional parameter demonstrating the optimum a_2/a_1 value for lowest simulated (AR$_{\min}$) and compared to that corresponding the measured AR$_{\text{measured}}$. The red solid line is a polynomial fit as a guide for the eyes. (b) Electromagnetic simulation of AR and S_{11} using the actual dimensions of sample 1.

expand remarkably, and a sharp increase in AR is observed; this is in addition to the synchronization frequency range obtained through experiments.

In accordance with the antenna theory, the minimum value of AR (AR_{min}) in a truncated edge patch antenna can be achieved when $a_2/a_1 = \sqrt{2Q_0} - 1$ [31,32]. Hence, the two main factors that contribute to the attainment of CP are the ratio a_2/a_1 and the quality factor (Q_0). Results of the electromagnetic simulation indicate that the existence of an optimum value of a_2/a_1 that corresponds to the lowest value of AR_{min}. Figure 4(a) depicts the variation in AR_{min}, including the values calculated in accordance with the preconditions mentioned in Sec. II B as well as those obtained experimentally in this study, as a function of a_2/a_1. The disagreement between optimum values of the ratio a_2/a_1 determined through simulation and experimental measurements may be attributed to the use of a simplified model. The value of Q_0, estimated from experimental results is 13 and that calculated through simulations is 36. The former value includes the ambiguity of dimensions on account of the trapezoidal shape of the mesa in addition to intrinsic material parameters, such as refractive index and surface impedance, which strongly influence the calculated value of Q_0.

Figure 5 depicts the emission spectra obtained for sample 3. Experimentally obtained AR as a function of the measured emission frequency, along with numerically calculated AR is plotted in Fig. 2(b). The observed deviation from model calculation is believed to have been by reasons similar to the ones mentioned in the preceding paragraph. The measured frequency range (0.435–0.457 THz) closely agrees with the estimated modal frequency for geometries occupying the top of the mesa stack [50]. Also, similar to the case illustrated above, V_b is found to be considerably higher than its value predicted using the emission frequency. This is believed to be due to excess voltage along the ab plane accompanied by the nucleation of hot spots [51], as depicted in Fig. S1 in the Supplemental Material [52]. Accordingly, the measurement of electric potential at the edges may result in higher values of the estimated Josephson frequency. Asymmetric electrode positions and emissions corresponding to the backbending region of the IVC may also yield similar results as frequency estimation is also affected by Joule heating [50]. Frequency measurements performed for sample 3 and previously published experimental results [38] indicate that electromagnetic simulations can be used to identify cavity resonant frequencies. Figure 4(b) depicts the variation of the scattering parameter (S_{11}) (blue line) and AR (red line) with the frequency of emission for sample 1. On the basis of these results, the resonant frequencies for sample 1 are estimated as $f_1 = 402$ GHz and $f_2 = 434$ GHz.

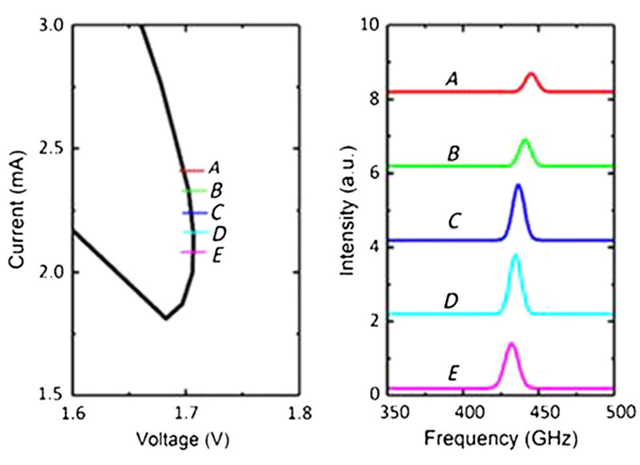

FIG. 5. Part of IVC (left) and emission spectra (right) of sample 3. Symbols marked A–E in the IVC represent bias conditions for respective spectra. Spectrum curves are vertically shifted to enable ease of visibility.

Recently, Asai and Kawabata predicted the emission of circularly polarized radiation from a slightly rectangular IJJ mesa, wherein the rise in local temperature was achieved through laser irradiation [25,36]. Their studies claim that LHCP is achieved when a corner, located on the left of the major bisector and facing the center ("A"), is irradiated by laser radiation. By the same reasoning, RHCP would be achieved when the adjacent corner (either "D" or "G") is heated. These results suggest that the in-plane superconducting current of the mesa surface, which causes a propagating electric field in the space, rotates in the direction defined by an arbitrary vector that starts from the point of irradiation and ends at the major bisector of the rectangular mesa (counterclockwise and clockwise current rotations observed at points A and D, respectively). In the experiments conducted in this study, the current electrode provides heat to the mesa and ends up performing a function similar to that performed by laser irradiation in the above study. In the proposed study, sample 1 exhibits a similar trend in terms of shape and heating as the model used in the above-mentioned study. This similarity could be attributed to the fact that the heating portion is located on the right of the major (untruncated) diagonal of the mesa (facing the center of the mesa). Therefore, in sample 1 (truncated left edge), we consider that the in-plane current rotates counterclockwise; therefore, LHCP radiation is obtained under a bias of 7–10 mA. For the same reasons, the electric field generated using sample 2 [Fig. 1(b)] is left handed and that generated using sample 3 (truncated right edge) is right handed. Thus, the direction of polarization rotation predicted for the truncated-edge square mesa is opposite to that estimated by antenna theory for a similarly shaped antenna fed at the same position.

In order to better understand the progression of polarization over the entire bias current range, plots in Figs. 6(a) and 6(b) depict the observed current-dependent intensity distribution in the form of a false-colored 2D contour plot for samples 1 and 3, respectively. As can be realized in Fig. 6(a), the maximum emission intensity is achieved in the minimum AR (best CP) at the current range of

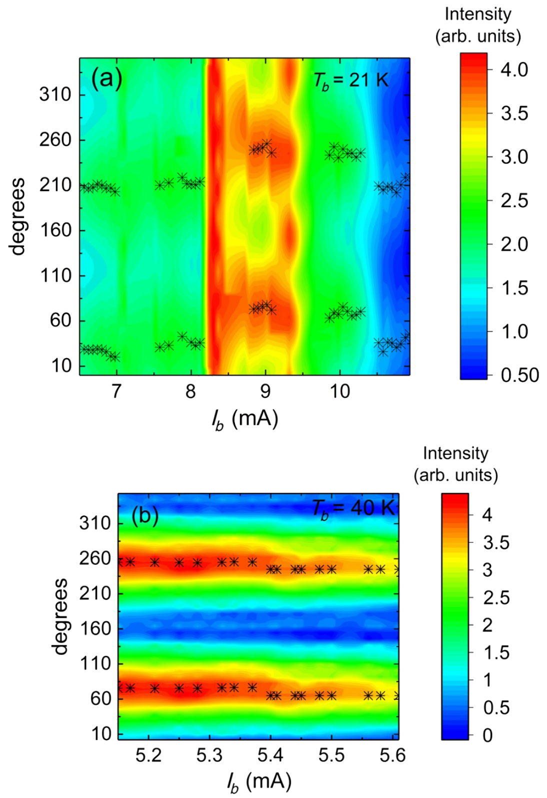

FIG. 6. Measured current- and angular-dependent intensities for the entire emission range of (a) sample 1 and (b) sample 3. The major axis angles corresponding to higher values of AR (>1 dB) are represented by asterisks.

8.3–8.5 mA; however, a rather low intensity is observed at the other low AR point (7 mA). In sample 1, the maxima of intensity correspond to the minimum values of AR (<1 dB). It is also observed that the angle of the major axis, indicated by an asterisk, is independent of I_b. Considering that the observed emission is a superposition of the two circular polarized modes (RHCP and LHCP), the AR evolution could be attributed to the variation in amplitudes of the two circularly polarized modes with a constant phase difference between them. Some minor fluctuations in the measured angle of the major axis angle are noticed in sample 1, which correspond to a small change in magnitude of the transverse mode owing to the imperfect shape of the edges. This fluctuation is less noticeable in sample 3 [Fig. 6(b)]. The authors intend to investigate this issue in detail in a future endeavor.

IV. CONCLUSIONS

This paper presents the design, fabrication, and experimental demonstration of a technique to generate circularly polarized terahertz radiations that comprise low axial ratios and maintain a high output intensity through the use of an intrinsic Josephson-junction oscillator. Circular polarization is achieved by using a simple truncated-edge square mesa structure. It verifies the simplicity and applicability of the antenna theory alongside the existing electromagnetic simulation methods in achieving the desirable polarization. Furthermore, because the proposed method is based on the excitation of IJJs within a mesa cavity, it avoids issues with the insertion loss associated with external polarimetric modulators, which may be substantial in the terahertz frequency range. The polarization characteristics have been discussed at length in terms of both the antenna theory as well as electromagnetic simulations. These results pave the way for the development of enhanced circularly polarized sources of terahertz radiation for use in practical applications, such as mobile communications and circular dichroism spectroscopy.

ACKNOWLEDGMENTS

The authors acknowledge the technical support from F. Tubbal, and would like to thank K. Kadowaki, T. Kashiwagi, H. Asai, S. Kawabata, H. Minami, S. Komori, Y. Nomura, R. Morita, S. Dhillon, and J. Tignon for the fruitful discussions. The Bi-2212 single crystals are provided by Y. Nakagawa and Y. Nomura. This work has been supported by KAKENHI No. 26286006 and Murata Science Foundation.

[1] M. Tonouchi, Cutting-edge terahertz technology, Nat. Photonics **1**, 97 (2007).

[2] L. Ozyuzer, A. E. Koshelev, C. Kurter, N. Gopalsami, Q. Li, M. Tachiki, K. Kadowaki, T. Yamamoto, H. Minami, H. Yamaguchi, T. Tachiki, K. E. Gray, W.-K. Kwok, and U. Welp, Emission of coherent THz radiation from superconductors, Science **318**, 1291 (2007).

[3] U. Welp, K. Kadowaki, and R. Kleiner, Superconducting emitters of THz radiation, Nat. Photonics **7**, 702 (2013).

[4] I. Kakeya and H. Wang, Terahertz-wave emission from Bi2212 intrinsic Josephson junctions: A review on recent progress, Supercond. Sci. Technol. **29**, 073001 (2016).

[5] D. P. Cerkoney, C. Reid, C. M. Doty, A. Gramajo, T. D. Campbell, M. A. Morales, K. Delfanazari, M. Tsujimoto, T. Kashiwagi, T. Yamamoto, C. Watanabe, H. Minami, K. Kadowaki, and R. A. Klemm, Cavity mode enhancement of terahertz emission from equilateral triangular microstrip antennas of the high-T_c superconductor $Bi_2Sr_2CaCu_2O_{8+\delta}$, J. Phys. Condens. Matter **29**, 015601 (2017).

[6] J. Xu, G. J. Ramian, J. F. Galan, P. G. Savvidis, A. M. Scopatz, R. R. Birge, S. J. Allen, and K. W. Plaxco, Terahertz circular dichroism spectroscopy: A potential approach to the *in situ* detection of life's metabolic and genetic machinery, Astrobiology **3**, 489 (2003).

[7] E. Castro-Carmiis, J. Lloyd-Hughes, M. B. Johnston, M. D. Fraser, H. H. Tan, and C. Jagadish, Polarization-sensitive terahertz detection by multicontact photoconductive receivers, Appl. Phys. Lett. **86**, 254102 (2005).

[8] P. Doradla, K. Alavi, C. Joseph, and R. Giles, Detection of colon cancer by continuous-wave terahertz polarization imaging technique, J. Biomed. Opt. **18**, 090504 (2013).

[9] G. Liang, Y. Zeng, X. Hu, H. Yu, H. Liang, Y. Zhang, L. Li, A. G. Davies, E. H. Linfield, and Q. J. Wang, Monolithic semiconductor lasers with dynamically tunable linear-to-circular polarization, ACS Photonics **4**, 517 (2017).

[10] P. Rauter, J. Lin, P. Genevet, S. P. Khanna, M. Lachab, A. Giles Davies, E. H. Linfield, and F. Capasso, Electrically pumped semiconductor laser with monolithic control of circular polarization, Proc. Natl. Acad. Sci. U.S.A. **111**, E5623 (2014).

[11] D. Horikawa, S. Suzuki, and M. Asada, in *Proceedings of the 2016 41st International Conerence on. Infrared, Millimeter, Terahertz Waves* (IEEE, New York, 2016), p. 1–2.

[12] H. B. Wang, S. Guénon, J. Yuan, A. Iishi, S. Arisawa, T. Hatano, T. Yamashita, D. Koelle, and R. Kleiner, Hot Spots and Waves in $Bi_2Sr_2CaCu_2O_{8+\delta}$ Intrinsic Josephson Junction, Phys. Rev. Lett. **102**, 0017006 (2009).

[13] M. Tsujimoto, H. Kambara, Y. Maeda, Y. Yoshioka, Y. Nakagawa, and I. Kakeya, Dynamic Control of Temperature Distributions in Stacks of Intrinsic Josephson Junctions in $Bi_2Sr_2CaCu_2O_{8+\delta}$, Phys. Rev. Applied **2**, 044016 (2014).

[14] H. Asai and S. Kawabata, Control of circularly polarized THz wave from intrinsic Josephson junctions by local heating, Appl. Phys. Lett. **110**, 132601 (2017).

[15] X. J. Zhou, J. Yuan, H. Wu, Z. S. Gao, M. Ji, D. Y. An, Y. Huang, F. Rudau, R. Wieland, B. Gross, N. Kinev, J. Li, A. Ishii, T. Hatano, V. P. Koshelets, D. Koelle, R. Kleiner, H. B. Wang, and P. H. Wu, Tuning the Terahertz Emission Power of an Intrinsic Josephson-Junction Stack with a Focused Laser Beam, Phys. Rev. Applied **3**, 044012 (2015).

[16] H. Minami, I. Kakeya, H. Yamaguchi, T. Yamamoto, and K. Kadowaki, Characteristics of terahertz radiation emitted from the intrinsic Josephson junctions in high-T_c superconductor $Bi_2Sr_2CaCu_2O_{8+\delta}$, Appl. Phys. Lett. **95**, 232511 (2009).

[17] M. Tsujimoto, K. Yamaki, K. Deguchi, T. Yamamoto, T. Kashiwagi, H. Minami, M. Tachiki, K. Kadowaki, and R. A. Klemm, Geometrical Resonance Conditions for THz Radiation from the Intrinsic Josephson Junctions in $Bi_2Sr_2CaCu_2O_{8+\delta}$, Phys. Rev. Lett. **105**, 037005 (2010).

[18] A. Constantine Balanis, *Antenna theory: Analysis and design*, 3rd ed. (John Wiley & Sons, New York, 2005).

[19] M. Leone, The radiation of a rectangular power-bus structure at multiple cavity-mode resonances, IEEE Transactions on Electromagnetic Compatibility **45**, 486 (2003).

[20] L. N. Bulaevskii and A. E. Koshelev, Radiation due to Josephson Oscillations in Layered Superconductors, Phys. Rev. Lett. **99**, 057002 (2007).

[21] A. E. Koshelev, Alternating dynamic state self-generated by internal resonance in stacks of intrinsic Josephson junctions, Phys. Rev. B **78**, 174509 (2008).

[22] S. Lin, X. Hu, and M. Tachiki, Computer simulation on terahertz emission from intrinsic Josephson junctions of high-T_c superconductors, Phys. Rev. B **77**, 014507 (2008).

[23] X. Hu and S. Lin, Three-dimensional phase-kink state in a thick stack of Josephson junctions and terahertz radiation, Phys. Rev. B **78**, 134510 (2008).

[24] S. Lin and X. Hu, Phase dynamics in intrinsic Josephson junctions and their electrodynamics, Phys. Rev. B **79**, 104507 (2009).

[25] H. Asai and S. Kawabata, Emission of circularly polarized terahertz wave from inhomogeneous intrinsic Josephson junctions, IEEE Trans. Appl. Supercond. **26**, 1800804 (2016).

[26] A. Elarabi, Y. Yoshioka, M. Tsujimoto, Y. Nakagawa, and I. Kakeya, Polarization enhancement of terahertz radiation generated by intrinsic josephson junctions in a truncated edge square $Bi_2Sr_2CaCu_2O_{8+\delta}$ mesa, Phys. Procedia **81**, 133 (2016).

[27] L. Xu, D. Chen, C. A. Curwen, M. Memarian, J. L. Reno, T. Itoh, and B. S. Williams, Metasurface quantum-cascade laser with electrically switchable polarization, Optica **4**, 468 (2017).

[28] M. Tsujimoto, T. Doi, G. Kuwano, A. Elarabi, and I. Kakeya, Engineering and characterization of a packaged high-T_c superconducting terahertz source module, Supercond. Sci. Technol. **30**, 064001 (2017).

[29] L. Y. Hao, M. Ji, J. Yuan, D. Y. An, M. Y. Li, X. J. Zhou, Y. Huang, H. C. Sun, Q. Zhu, F. Rudau, R. Wieland, N. Kinev, J. Li, W. W. Xu, B. B. Jin, J. Chen, T. Hatano, V. P. Koshelets, D. Koelle, R. Kleiner, H. B. Wang, and P. H. Wu, Compact Superconducting Terahertz Source Operating in Liquid Nitrogen, Phys. Rev. Applied **3**, 024006 (2015).

[30] K. Nakade, T. Kashiwagi, Y. Saiwai, H. Minami, T. Yamamoto, R. A. Klemm, and K. Kadowaki, Applications using high-T_c superconducting terahertz emitters, Sci. Rep. **6**, 23178 (2016).

[31] M. Haneishi and S. Yoshida, A design method of circularly polarized rectangular microstrip antenna by one-point feed, Electron. Commun. Jpn. 2, Electron. **64**, 46 (1981).

[32] M. Haneishi and Y. Suzuki, in *Handbook of Microstrip Antennas*, edited by J. R. James and P. S. Hall (The Institution of Engineering and Technology, Stevenage, U.K., 1989), Vol. 1, pp. 219–274.

[33] M. I. Ali, K. Ehata, and S. Ohshima, Single-feed superconducting circularly polarized microstrip array antenna for direct-to-home receiving system, Supercond. Sci. Technol. **13**, 1095 (2000).

[34] R. A. Sainati, *CAD of Microstrip Antennas for Wireless Applications* (Artech House, 1996).

[35] H. Asai and S. Kawabata, Intense terahertz emission from intrinsic Josephson junctions by external heat control, Appl. Phys. Lett. **104**, 112601 (2014).

[36] H. Asai and S. Kawabata, Control of circularly polarized THz wave from intrinsic Josephson junctions by local heating, Appl. Phys. Lett. **110**, 132601 (2017).

[37] S. Gao, Q. Luo, and F. Zhu, *Circularly Polarized Antennas* (John Wiley & Sons, Ltd., Chichester, U.K., 2014).

[38] M. Tsujimoto, I. Kakeya, T. Kashiwagi, H. Minami, and K. Kadowaki, Cavity mode identification for coherent terahertz emission from high-T_c superconductors, Opt. Express **24**, 4591 (2016).

[39] K. Berggren and D. Aude, *Modeling Superconductors Using Surface Impedance Techniques* (Massachusetts Institute of Technology, Cambridge, MA, 2010).

[40] W. Zimmermann, E. H. Brandt, M. Bauer, E. Seider, and L. Genzel, Optical conductivity of BCS superconductors with arbitrary purity, Physica (Amsterdam) **183C**, 99 (1991).

[41] S.-F. Lee, D. Morgan, R. Ormeno, D. Broun, R. Doyle, J. Waldram, and K. Kadowaki, *a-b* Plane Microwave Surface

Impedance of a High-Quality $Bi_2Sr_2CaCu_2O_{8+\delta}$ Single Crystal, Phys. Rev. Lett. **77**, 735 (1996).

[42] A. Yariv and P. Yeh, *Photonics: Optical Electronics in Modern Communications* (Oxford University Press, New York, 2007).

[43] I. Kakeya, N. Hirayama, T. Nakagawa, Y. Omukai, and M. Suzuki, Temperature and current dependencies of terahertz emission from stacks of intrinsic Josephson junctions with thin electrodes revealed by a high-resolution FT-IR spectrometer, Physica (Amsterdam) **491C**, 11 (2013).

[44] K. Kadowaki, H. Yamaguchi, K. Kawamata, T. Yamamoto, H. Minami, I. Kakeya, U. Welp, L. Ozyuzer, A. Koshelev, C. Kurter, K. E. Gray, and W.-K. Kwok, Direct observation of tetrahertz electromagnetic waves emitted from intrinsic Josephson junctions in single crystalline $Bi_2Sr_2CaCu_2O_{8+\delta}$, Physica (Amsterdam) **468C**, 634 (2008).

[45] T. Kashiwagi, K. Yamaki, M. Tsujimoto, K. Deguchi, N. Orita, T. Koike, R. Nakayama, H. Minami, T. Yamamoto, R. A. Klemm, M. Tachiki, and K. Kadowaki, Geometrical full-wavelength resonance mode generating terahertz waves, J. Phys. Soc. Jpn. **80**, 094709 (2011).

[46] T. M. Benseman, K. E. Gray, A. E. Koshelev, W.-K. Kwok, U. Welp, H. Minami, K. Kadowaki, and T. Yamamoto, Powerful terahertz emission from $Bi_2Sr_2CaCu_2O_{8+\delta}$ mesa arrays, Appl. Phys. Lett. **103**, 022602 (2013).

[47] S. Guénon, M. Grünzweig, B. Gross, J. Yuan, Z. G. Jiang, Y. Y. Zhong, M. Y. Li, A. Iishi, P. H. Wu, T. Hatano, R. G. Mints, E. Goldobin, D. Koelle, H. B. Wang, and R. Kleiner, Interaction of hot spots and terahertz waves in $Bi_2Sr_2CaCu_2O_{8+\delta}$ intrinsic Josephson junction stacks of various geometry, Phys. Rev. B **82**, 214506 (2010).

[48] See Supplemental Material at http://link.aps.org/supplemental/10.1103/PhysRevApplied.8.064034 for the calculation of the degree of circular polarization.

[49] R. A. Klemm and K. Kadowaki, Output from a Josephson stimulated terahertz amplified radiation emitter, J. Phys. Condens. Matter **22**, 375701 (2010).

[50] T. M. Benseman, A. E. Koshelev, W.-K. Kwok, U. Welp, K. Kadowaki, J. R. Cooper, and G. Balakrishnan, The ac Josephson relation and inhomogeneous temperature distributions in large $Bi_2Sr_2CaCu_2O_{8+\delta}$ mesas for THz emission, Supercond. Sci. Technol. **26**, 085016 (2013).

[51] C. Watanabe, H. Minami, T. Kitamura, Y. Saiwai, Y. Shibano, T. Katsuragawa, H. Kubo, K. Sakamoto, T. Kashiwagi, R. A. Klemm, and K. Kadowaki, Electrical potential distribution in terahertz-emitting rectangular mesa devices of high-T_c superconducting $Bi_2Sr_2CaCu_2O_{8+\delta}$, Supercond. Sci. Technol. **29**, 065022 (2016).

[52] See Supplemental Material at http://link.aps.org/supplemental/10.1103/PhysRevApplied.8.064034 for a schematic figure showing the formation of a hot spot under the bias electrode caused by the in-plane resistance of the locally heated region.

Superconductor Science and Technology

PAPER

Negative correlation between enhanced crossover temperature and fluctuation-free critical current of the second switch in $Bi_2Sr_2CaCu_2O_{8+\delta}$ intrinsic Josephson junction

To cite this article: Y Nomura *et al* 2017 *Supercond. Sci. Technol.* **30** 105001

Supercond. Sci. Technol. **30** (2017) 105001 (7pp) https://doi.org/10.1088/1361-6668/aa7b23

Negative correlation between enhanced crossover temperature and fluctuation-free critical current of the second switch in $Bi_2Sr_2CaCu_2O_{8+\delta}$ intrinsic Josephson junction

Y Nomura, R Okamoto and I Kakeya

Department of Electronic Science and Engineering, Kyoto University, Katsura, Nishikyo-ku, Kyoto 615-8510, Japan

E-mail: nomura@sk.kuee.kyoto-u.ac.jp

Received 20 January 2017, revised 10 May 2017
Accepted for publication 22 June 2017
Published 21 August 2017

Abstract

We have investigated the switching dynamics of the first and second switches in intrinsic Josephson junctions (IJJs) of $Bi_2Sr_2CaCu_2O_{8+\delta}$ with different maximum Josephson current density J_c to reveal the doping evolution of interaction between IJJs. For the second switch, the crossover temperature between temperature-independent switching similar to quantum tunneling and thermally activated switching T^*_{2nd} is remarkably higher than that for the first switch. Moreover, T^*_{2nd} slightly decreases with increasing J_c, which violates the conventional relation between the crossover temperature and the critical current density. These features can be explained not by a change in the Josephson coupling energy but by a change in the charging energy of the Josephson junction. We argue that the capacitive coupling model explains the increase in the fluctuation in the quantum regime of the second switch and the anti-correlation between T^*_{2nd} and J_c. Furthermore, inductive coupling does not contribute to these peculiar phenomena in the switching dynamics of stacked IJJs.

Keywords: intrinsic Josephson junction, Bi2212, macroscopic quantum tunneling, capacitive coupling

(Some figures may appear in colour only in the online journal)

1. Introduction

A rich variety of phenomena observed in intrinsic Josephson junctions (IJJs) included in anisotropic superconductors such as $Bi_2Sr_2CaCu_2O_{8+\delta}$ (Bi2212) has delivered various physical notions and suggestions for implementation in novel devices for more than 20 years [1–4]. In Bi2212, superconducting CuO_2 layer and insulating BiO layer are alternately stacked at the atomic scale. Couplings between the IJJs due to the thin superconducting CuO_2 layer cause various phenomena peculiar to IJJ stacks [5–10]. It is considered that the stacked IJJs are coupled both inductively and capacitively [11, 12]. The origin of the inductive coupling is the penetration of in-plane current over neighboring IJJs. A Josephson vortex lattice is a typical example of the result of the inductive coupling [8]. This effect can be embedded into the maximum Josephson current density J_c, which gives the Josephson coupling energy E_J. The inductive coupling is an essential ingredient for large-scale synchronization, such as terahertz radiation from IJJs [9, 10]. The origin of the capacitive coupling is breaking of the charge neutrality in the CuO_2 superconducting layer due to Josephson tunneling [13]. An effect of the capacitive coupling is represented by the change in charging energy E_c. It is simulated that the multiple-branched current–

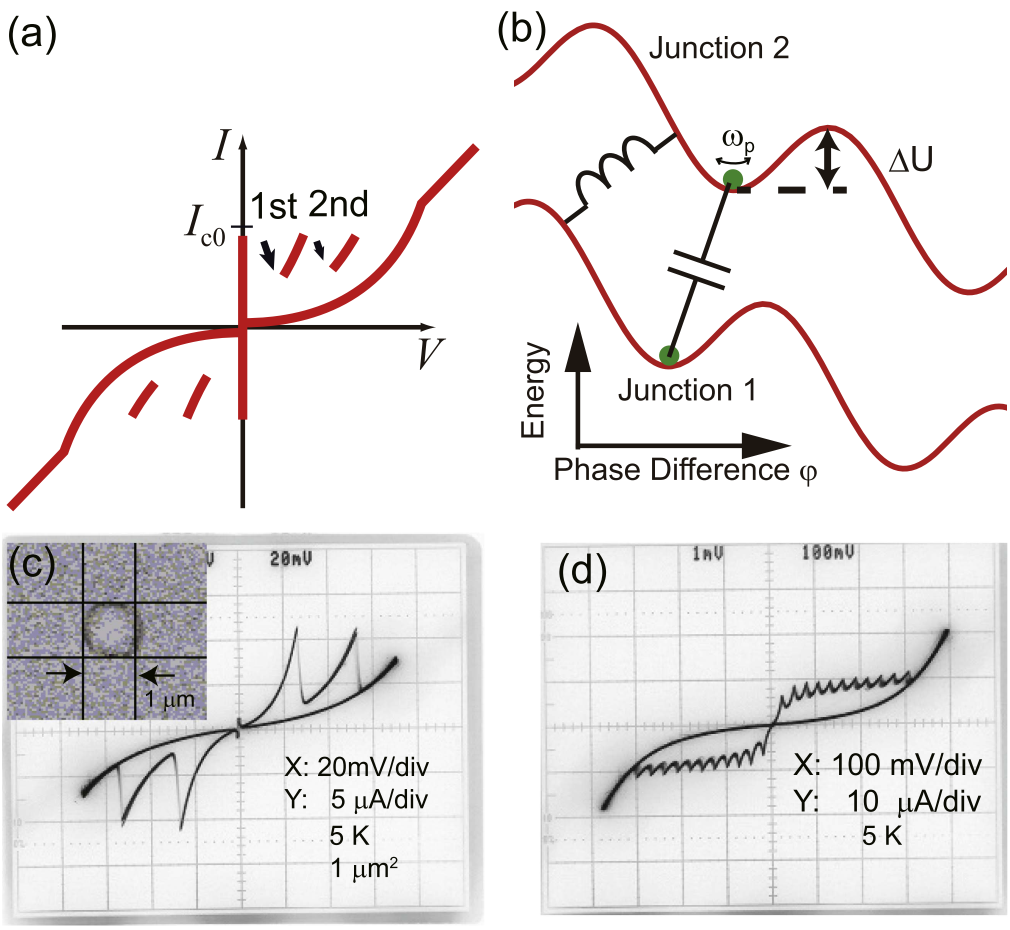

Figure 1. Schematic drawings of (a) the *I–V* characteristic of IJJ stack and (b) coupling between two IJJs [28]. It is noted that the vertical shift between the tilted washboard potentials in (b) does not mean a difference in energy. *I–V* characteristics of sample D at 5 K with (c) low-bias and (d) high bias current. The inset of (c) is a planar SEM image of an EB resist (rounded square) for sample D. The mesa with an approximate size of 1 μm^2 is formed underneath of the resist by subsequent Ar ion milling.

voltage (*I–V*) characteristics of IJJ stacks are caused by the capacitive coupling [14]. However, another explicit effect of the capacitive coupling has not been observed.

In this article, a switch from the supercurrent ($R = 0$) branch to the first resistive branch is referred to as the first switch and a switch from the first to the second resistive branch is referred to as the second switch, as shown in figure 1(a). For the first switch, the switching probability distribution *P*(*I*) and escape rate $\Gamma(I)$ agree with expectations given by the single junction model. Around 4 K, $\Gamma(I)$ indicates that thermal activation (TA) is dominant for the switch [15]. At sufficiently low temperatures, $\Gamma(I)$ does not depend on temperature; thus, macroscopic quantum tunneling (MQT) turns out to be dominant for the switch. The crossover between TA and MQT was found to be at $T^*_{1st} \sim 1$ K, which roughly corresponds to the theoretical crossover temperature $T_{cr} = \hbar\omega_p/\pi k_B$ estimated from the single junction model [16, 17], where ω_p is the Josephson plasma frequency under a bias current, k_B is the Boltzmann constant, and $\hbar = h/2\pi$ is the reduced Planck constant. In large size IJJ stacks, *P*(*I*) has multiple peaks and is broadened because of the inclusion of Josephson vortices [18, 19]. $\Gamma(I)$ in the MQT regime is significantly enhanced when a large number of IJJs switch simultaneously [20]. The origin of the large $\Gamma(I)$ for the simultaneous switch was argued in terms of the inductive coupling [21]. For the second switch, an MQT-like temperature-independent $\Gamma(I)$ was observed with the experimental crossover temperature T^*_{2nd}, which is much higher than the T_{cr} [22–24]. In our previous work, we claimed that the large T^*_{2nd} is attributed to charge coupling [24, 25]. A possible energy level quantization of the second switch up to 4 K has been reported by Takahashi *et al* [26]. In contrast, Warburton *et al* argued that switching currents of the second switches are significantly reduced by the suppression of the phase retrapping at TA regime in comparison with those of the first switch [27].

In this paper, we discuss the nature of capacitively and inductively coupled IJJs through measurements of *P*(*I*) in four Bi2212 samples with different critical current densities. The behavior of the first switch follows the single junction model as discussed in a previous report [16]. For the second switch, however, T^*_{2nd}'s were found to be higher than both T^*_{1st} and T_{cr}. In the TA regime, *P*(*I*)'s for both switches completely follow the TA model and E_J is equivalent to the value estimated from the single junction model. These results indicate that the

Table 1. Obtained parameters of the four samples. N is the number of stacked IJJs, determined by the number of branches found in the I–V characteristics. J_{c0}(1st), T^*_{1st}, J_{c0}(2nd) and T^*_{2nd} are obtained through the Kramers formula from experimental $P(I)$. T_{cr} is calculated as $T_{cr} = \hbar\omega_p/\pi k_B$ from J_{c0}. ΔU and ω_p are the height of the potential barrier and the plasma frequency at the most frequent switching current I_c. See the text.

Sample	A	B	C	D
N	13	12	12	12
$\mathrm{d}I/\mathrm{d}t$ (mA s^{-1})	0.80	2.5	2.6	2.3
J_{c0}(1st) (kA cm^{-2})	0.40	0.69	0.86	0.46
T^*_{1st} (K)	0.86	2.2	1.4	1.2
T_{cr}(1st) (K)	0.39	0.48	0.52	0.41
J_{c0}(2nd) (kA cm^{-2})	1.0	1.4	1.8	1.9
T^*_{2nd} (K)	8.1	7.4	6.8	6.7
T_{cr}(2nd) (K)	0.54	0.63	0.71	0.72
$\Delta U/h$ (GHz)	2690	2520	2440	2330
$\omega_p/2\pi$ (GHz)	581	653	710	723

increase in T^*_{2nd} is not explained by the inductive coupling. Furthermore, we found that T^*_{2nd} decreases with increasing fluctuation-free critical current density J_{c0}. This negative correlation is explained by the capacitive coupling because the strength of the capacitive coupling is considered to be weakened by increasing J_{c0}. Our results suggest that the change in the inductive coupling is negligible for the second switch and that the capacitive coupling is relevant for the enhancement of the fluctuation of the second switch.

2. Experiment and data analysis

In the present study, we discuss results in four mesa devices (A to D) made of an as-grown Bi2212 single crystal prepared in the following procedure. The Bi2212 single crystal was grown by the traveling-solvent floating zone method. The nominal composition is $Bi_{2.15}Sr_{1.85}Ca_{1.0}Cu_{2.0}O_{8+\delta}$. In the beginning, the crystal was cleaved in a vacuum to get a clean surface and to reduce the contact resistance. Subsequently, Ag for the electrodes was deposited with a thickness of 400 Å in vacuum. The Ag electrode capping of the mesa has the advantage of preventing self-heating of the IJJs. On the surface of the Bi2212 single crystal capped by the thick Ag, four mesa structures with a size of $1 \times 1\ \mu\mathrm{m}^2$ were formed by electron-beam (EB) lithography and Ar ion milling. The inset of figure 1(c) is a scanning electron microscope image of an EB resist before the Ar ion milling. The details of the sample preparation process are described elsewhere [29].

The samples were cooled to 0.4 K with a ^{3}He cryostat and their $P(I)$ was measured by a time-of-flight method [30]. The ramp current was biased into the IJJs by a constant-current source. The ramp rate $\mathrm{d}I/\mathrm{d}t$ is common in both the first and second switches and $\mathrm{d}I/\mathrm{d}t$ in each sample is listed in table 1. To reduce the self-heating, the bias current becomes zero immediately after either the first switch or the second switch. Great cares for noise reduction such as electrical isolations of measurement system from digital equipment, low temperature filters, and so on have been paid according to the general protocols for macroscopic quantum measurements [31, 32]. We obtained $P(I)$ as a histogram of switching current for 10 000 current ramps, and $\Gamma(I) = \Delta I^{-1}\mathrm{d}I/\mathrm{d}t\ \ln[\Sigma_{i>I}P(i)/\Sigma_{i>I-\Delta I}P(i)]$. The details of the measurement setup are described in [25, 33].

The acquired data are analyzed according to the resistively and capacitively shunted junction (RCSJ) model, which is mechanically analogized by a phase particle inside a tilted washboard potential. Stacked IJJs can be considered as a series of sets of a washboard and a particle. The coupling between IJJs is depicted by the interaction between either washboards or particles. Figure 1(b) presents a schematic drawing of the couplings [28]. The height of the potential is modified by inductive coupling, whereas the effective mass of the particle is modified by capacitive coupling because the effective mass depends on the capacitance of the RCSJ model. In conventional Josephson junctions, TA and MQT rates are respectively formulated as

$$\Gamma_{TA} = \frac{\omega_p}{2\pi}\exp\left(-\frac{\Delta U}{k_B T}\right), \tag{1}$$

$$\Gamma_{MQT} = \frac{\omega_p}{2\pi}\left(\frac{864\pi\Delta U}{\hbar\omega_p}\right)^{\frac{1}{2}}\exp\left(-\frac{36\Delta U}{5\hbar\omega_p}\right), \tag{2}$$

where ΔU is the height of a potential barrier in the tilted washboard model, and T is temperature [34, 35]. $\omega_p = \sqrt{2E_c E_J}/\hbar\cdot(1-\gamma^2)^{1/4}$ depends on both E_c and E_J, whereas $\Delta U = 2E_J(\sqrt{1-\gamma^2} - \gamma\arccos\gamma)$ depends only on E_J, where γ is the bias current I divided by the fluctuation-free critical current I_{c0}. Thus, measuring $\Gamma(I)$ is suitable for acquiring the change in E_c and E_J: Γ_{TA} increases with increasing T, Γ_{MQT} increases with increasing E_c, and both Γ_{TA} and Γ_{MQT} increase with decreasing E_J. In this study, we derived the effective temperature T_{eff} to quantify the magnitude of the fluctuations. T_{eff} is obtained by fitting equation (1) to $\Gamma(I)$ with regarding $T_{eff} = T$.

3. Results and discussion

Figures 1(c) and (d) show the I–V characteristics of sample D at $T = 5$ K with a low-bias current to display the supercurrent branch and a high bias current to display all resistive branches, respectively. The maximum currents of the supercurrent and the first resistive branches are 2.0 and 12 μA. The magnitudes of the voltage separations at $I = 12\ \mu$A between adjacent branches are almost equal to 24 mV. Counting the number of branches in figure 1(d) enables the determination of the number of the stacked IJJs N. It is known that J_c of the first (topmost) IJJ is often decreased remarkably because of the proximity effect of the Ag electrode [36]. This means that the first IJJ definitely turns to the resistive state at the first switch. This suppression makes the distinction of the first switch and the second switch much easier. Thus, the second

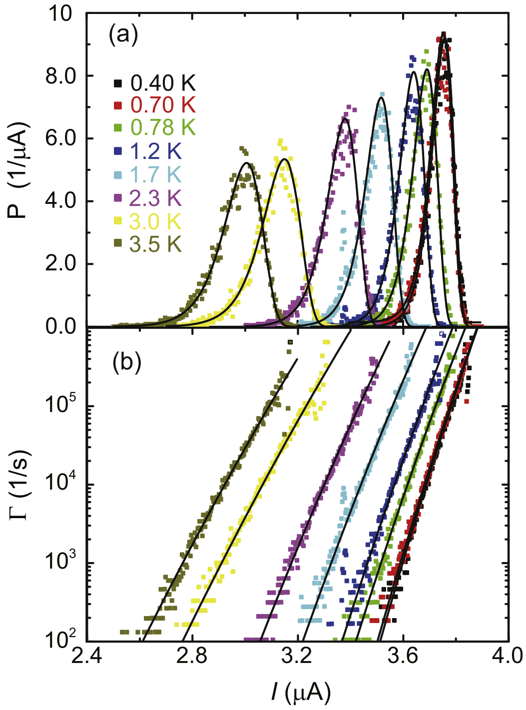

Figure 2. Switching probability distributions $P(I)$ and escape rates $\Gamma(I)$ of the first switch (a), (b) and the second switch (c), (d) in sample D. Solid curves are the fitting results of the Kramers formula equation (1).

(topmost) IJJ presumably turns to the resistive state at the second switch.

$P(I)$ and $\Gamma(I)$ for the first and second switches of sample D are shown in figure 2. $P(I)$ and $\Gamma(I)$ of the first switch below 0.7 K are almost identical. $P(I)$ is broadened and the switching current decreases with increasing bath temperature T_{bath} above 0.7 K. For the second switch, $P(I)$ and $\Gamma(I)$ are temperature-independent below 2 K. Then, $P(I)$ is broadened and the switching current decreases with increasing T_{bath}.

Figure 3(a) shows T_{eff} versus T_{bath} plots for four samples. For the first switch of sample D, T_{eff} almost equals T_{bath} above 1.8 K and starts to deviate from $T_{\mathrm{eff}} = T_{\mathrm{bath}}$ with decreasing T_{bath}. In this temperature region, TA is dominant for switching. Finally, T_{eff} becomes independent of T_{bath} below 0.7 K, where quantum tunneling is dominant for switching. T^*_{1st} is determined by the crossing between constant T_{eff} and $T_{\mathrm{eff}} = T_{\mathrm{bath}}$ as 1.2 K for sample D. For the second switch, we found $T_{\mathrm{eff}} \simeq T_{\mathrm{bath}}$ above 10 K and T_{eff} independent of T_{bath} below 4 K; then, $T^*_{\mathrm{2nd}} = 6.7$ K was obtained. The J_{c0} is 0.46 kA cm^{-2} (for the first switch) and 1.9 kA cm^{-2} (for the second switch) at sufficiently low temperatures. Theoretical crossover temperatures T_{cr} estimated from J_{c0} are 0.41 and 0.72 K and their decreases from the experimental crossover temperatures are 0.8 and 6.0 K for the first and the second switches, respectively. Temperature dependence of J_{c0} and the most frequent switching current density (J_{sw}), derived from a bias current where $P(I)$ gives the maximum, are shown in figure 3(b). Both of the J_{c0}'s little depend on T_{bath} in this temperature range while the J_{sw} decreases with increasing T_{bath} as shown in figure 3(b). These parameters obtained in all four samples are summarized in table 1. The difference in J_{c0} is originally attributed to a slight distribution of cation chemical compositions in the crystal yielded during the crystal growth.

It turns out that the increases of T^*_{1st} from T_{cr} were found to be less than 1.8 K whereas those of T^*_{2nd} are more than 6.0 K. We consider that the slight increase in the T^*_{1st} is due to external white noise, which cannot be removed by filtering the signal wires. It was found that this remarkable increase of T^*_{2nd} in comparison to T^*_{1st} and T_{cr} is a common feature for IJJ stacks of Bi2212. To illuminate the peculiarities of the second switch, a non-trivial J_{c0} evolution of T^*_{2nd} is presented in figure 4. The T^*_{2nd} decreases with increasing J_{c0}, which is in sharp contrast to the expectation of the single junction model shown by a solid line indicating T_{cr}. This result explicitly supports the argument to rule out the possibility of the heating origin of the T^*_{2nd} increase in addition to reasons suggested in previous reports [25, 37]. If the temperature rise of the second IJJ due to the resistive state of the first IJJ were essential, T^*_{2nd} would be higher in a sample with higher J_{c0}(2nd). Moreover, numerical simulations on the heating effect of the biased mesa structure have revealed that temperature rise is negligible for the results. Suzuki *et al* have pointed that the temperature rise is less than 0.6 K for the second switch of a mesa device with $J_{c0} = 2.0$ kA cm^{-2}, a dimension of $2 \times 2\ \mu$m^2, and the same electrode thickness [38]. This is much smaller than the increase of T^*_{2nd} from T_{cr}(2nd) despite that the J_{c0} and the dimension are considerably larger than those in the present study. Therefore, the heating effect is not relevant for the increase of T^*_{2nd}. It also turns out that the effect of environmental noise is not essential. If we assume that the deviation of T^*_{1st} from T_{cr}

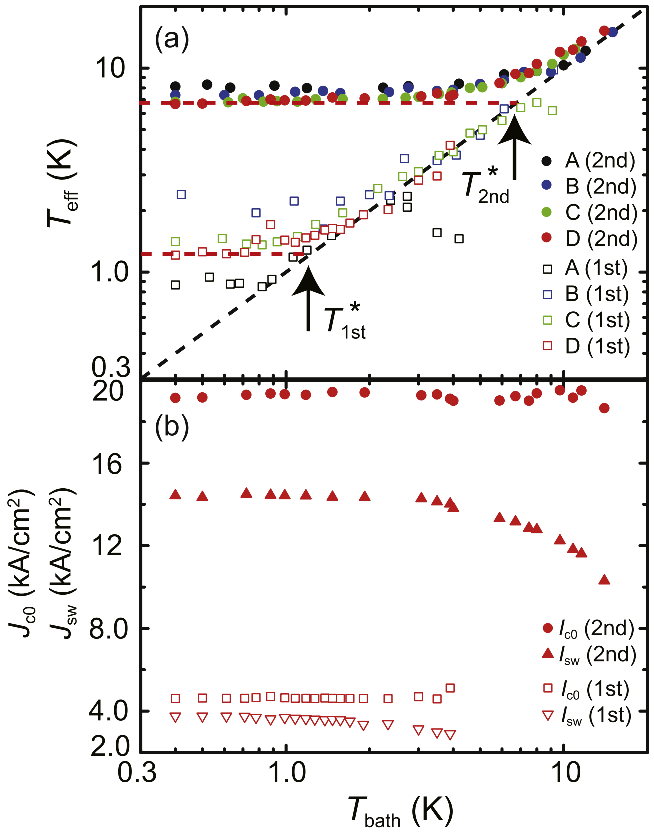

Figure 3. (a) Plots of the effective temperature T_{eff} versus the bath temperature T_{bath} of the first and the second switches in all samples. Lower and upper arrows respectively point crossover temperatures of the first and the second switches of sample D. (b) Temperature dependence of the fluctuation-free critical current density J_{c0} and the most frequent switching current density J_{sw} of the first and the second switches of sample D.

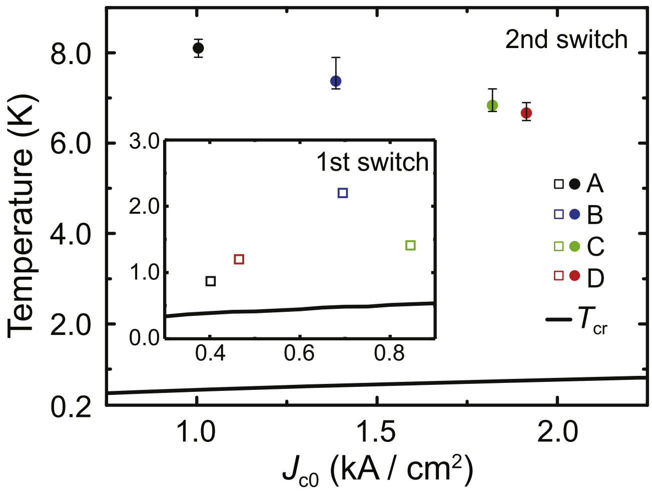

Figure 4. Plot of the experimental crossover temperature of the second switch T^*_{2nd} as a function of the fluctuation-free critical current J_{c0}. In the inset, the plot on T^*_{1st} is shown. Solid lines represent T_{cr} calculated from J_{c0}.

displayed in the inset of figure 4 is attributed to the external noise, the results of sample A is the least seriously suffered by the external noise. However, the deviation of T^*_{2nd} from T_{cr} is the maximum for the sample A and is inconsistent to the trend on T^*_{1st}. Thus we argue that this evolution of T^*_{2nd} can be explained by considering an inherent coupling effect between IJJs. In the following discussion, the origin of our finding on the second switch is described with respect to the coupling between IJJs.

First, we claim that the inductive coupling and the large junction effect are irrelevant to the second switch through the behavior of the TA regime of the first and second switches. We found that T_{eff} almost equals T_{bath} above 10 K for the second switch of four Bi2212 samples. This is interpreted as the thermal escape of the second switch being explained by the single junction model. It is noted that Γ_{TA} is dominated not by ω_{p} but by T and ΔU, which are included in the exponential term of equation (1). It has been reported that the inductive coupling decreases ΔU theoretically [28] and experimentally [18]. Therefore, it is concluded that the inductive coupling does not influence the second switch. This conclusion is also consistent with that from the discussion on the phase retrapping regime [39]. Moreover, the result $T_{\mathrm{eff}} = T_{\mathrm{bath}}$ of the second switch in the TA regime has been reported not only in Bi2212 [26, 40] but also in $\mathrm{Bi_2Sr_2CuO_{6+\delta}}$ [33]. In a large junction where the length of the junction L is considerably larger than the Josephson penetration depth λ_{J}, current density is not uniform over the junction because of the shielding effect. As a result, the height of the effective potential barrier is reduced by a factor of λ_{J}/L because of the self-field induced by the bias current [41, 42]. This effect adds a constant factor to T_{eff}, which is determined by λ_{J}/L, and ends in an upward parallel shift in a log–log plot of T_{eff} versus T_{bath}. In the present work, no parallel shift in the TA regime is found in figure 3(a); therefore, the large junction effect need not to be taken into account.

Then we discuss capacitive coupling as a possible origin of the enhancement of the T^*_{2nd} and its doping dependence. The strength of the capacitive coupling is represented by the coupling constant $\alpha = \epsilon_r \mu^2/sd$, where ϵ_r is the dielectric constant, μ is the charge screening length, s is the thickness of the superconducting layer and d is the thickness of the insulating layer [12]. In the present study, the chemical composition of the crystal, dimensions of the mesa structures, and numbers of IJJs are considered to be identical in all samples because they were fabricated on the same crystal simultaneously. Therefore, the ϵ_r, s and d can be regarded as the identical values. We consider that only μ is varied by doping. Let us estimate μ under the assumption of the Debye screening. The Debye screening length λ_{D} is given by the plasma frequency as $\lambda_{\mathrm{D}} = \sqrt{\epsilon_0 k_{\mathrm{B}} T/m}/\omega_{\mathrm{p}}$, where ϵ_0 and m are the vacuum dielectric constant and effective mass of an electron participating in the screening. Here, m can be assumed as $2m_{\mathrm{e}} \cdot m_{\mathrm{c}}/m_{ab}$ with the mass of a free electron m_{e} and superconducting anisotropy $\sqrt{m_{\mathrm{c}}/m_{ab}}$, which is 100 for the case of Bi2212. Using ω_{p} values at the most frequent switching current for samples as listed in table 1, μ and α are in the ranges from 0.0299 to 0.0241 nm and from 0.025 to 0.016 for A to D. Although these values are one-order smaller than values in the literature, the trend is consistent with the experimental results. Such a negative J_{c0} evolution of μ is also concluded by the assumption of the Thomas–Fermi screening of the superconducting charge [13]. The small α leads to weak enhancement of T^*_{2nd} because of the weak coupling. Therefore, the enhancement of T^*_{2nd} is attributed to the capacitive coupling between two adjacent, the first and the second IJJs.

A possible interpretation of the enhancement of T^*_{2nd} due to the capacitive coupling was suggested by Koyama [43]. When the second IJJ is switching to the resistive state, the first IJJ in the resistive state radiates an electromagnetic wave according to the AC Josephson relation. Because of the capacitive coupling, the radiated electromagnetic wave is exerted to the second IJJ and induces an escape from the trapped potential. Since the voltage of the first IJJ is approximately $V = 25$ mV as shown in figure 1(c), the Josephson frequency $\nu_J = 2\,\mathrm{eV}/h \sim 10$ THz is estimated. The corresponding energy is much higher than remaining height of the potential ΔU at the second switch as listed at the bottom row of table 1. Thus, a trapped phase particle is excited from the ground state to a continuous excited state as well as the photoelectric effect and escapes from the potential. We consider that this process presumably causes the significant enhancement of $\Gamma(I)$ in the second switch and results in a large T^*_{2nd}.

4. Conclusion

We measured the phase dynamics of stacked IJJs of Bi2212 coupled capacitively and inductively. The temperature dependence of T_{eff} for the first switch is explained by the single junction model. On the other hand, T^*_{2nd} is remarkably larger than T_{cr}, which is in agreement with previous reports. The present study shows that the second switch is explained by the TA model above 10 K. Thus E_J is identical to the value determined by the single junction model, which means the inductive coupling is irrelevant to the second switch in small-sized IJJ stacks. The negative correlation between T^*_{2nd} and J_{c0} is presumably due to the capacitive coupling. Our results suggest that capacitive coupling is relevant for the enhancement of the quantum fluctuation.

Acknowledgments

This work was partly supported by the JSPS KAKENHI Grant No. 16J11491. We thank Osamu Sakai at University of Shiga Prefecture for allowing us to use an electron-beam lithography facility.

ORCID iDs

Y Nomura https://orcid.org/0000-0002-5308-4696

References

[1] Kleiner R, Steinmeyer F, Kunkel G and Müller P 1992 *Phys. Rev. Lett.* **68** 2394
[2] Suzuki M and Watanabe T 2000 *Phys. Rev. Lett.* **85** 4787
[3] Krasnov V M, Yurgens A, Winkler D, Delsing P and Claeson T 2000 *Phys. Rev. Lett.* **84** 5860
[4] Kambara H, Kakeya I and Suzuki M 2013 *Phys. Rev.* B **87** 214521
[5] Kleiner R, Müller P, Kohlstedt H, Pedersen N F and Sakai S 1994 *Phys. Rev.* B **50** 3942
[6] Irie A, Hirai Y and Oya G 1998 *Appl. Phys. Lett.* **72** 2159
[7] Krasnov V M, Mros N, Yurgens A and Winkler D 1999 *Phys. Rev.* B **59** 8463
[8] Koshelev A E, Buzdin A I, Kakeya I, Yamamoto T and Kadowaki K 2011 *Phys. Rev.* B **83** 224515
[9] Ozyuzer L *et al* 2007 *Science* **318** 1291
[10] Kakeya I and Wang H 2016 *Supercond. Sci. Technol.* **29** 073001
[11] Sakai S, Bodin P and Pedersen N F 1993 *J. Appl. Phys.* **73** 2411–8
[12] Koyama T and Tachiki M 1996 *Phys. Rev.* B **54** 16183–91
[13] Machida M, Koyama T and Tachiki M 1999 *Phys. Rev. Lett.* **83** 4618
[14] Machida M and Koyama T 2004 *Phys. Rev.* B **70** 024523
[15] Krasnov V M, Bauch T and Delsing P 2005 *Phys. Rev.* B **72** 012512
[16] Inomata K, Sato S, Nakajima K, Tanaka A, Takano Y, Wang H B, Nagao M, Hatano H and Kawabata S 2005 *Phys. Rev. Lett.* **95** 107005
[17] Li S X, Qiu W, Han S, Wei Y F, Zhu X B, Gu C Z, Zhao S P and Wang H B 2007 *Phys. Rev. Lett.* **99** 037002
[18] Mros N, Krasnov V M, Yurgens A, Winkler D and Claeson T 1998 *Phys. Rev.* B **57** R8135
[19] Krasnov V, Oboznov V, Ryazanov V, Mros N, Yurgens A and Winkler D 2000 *Phys. Rev.* B **61** 766
[20] Jin X Y, Lisenfeld J, Koval Y, Lukashenko A, Ustinov A V and Müller P 2006 *Phys. Rev. Lett.* **96** 177003
[21] Savel'ev S, Rakhmanov A L and Nori F 2007 *Phys. Rev. Lett.* **98** 077002
[22] Kashiwaya H, Matsumoto T, Shibata H, Kashiwaya S, Eisaki H, Yoshida Y, Kawabata S and Tanaka Y 2008 *J. Phys. Soc. Japan* **77** 104708
[23] Ota K, Hamada K, Takemura R, Ohmaki M, Machi T, Tanabe K, Suzuki M, Maeda A and Kitano H 2009 *Phys. Rev.* B **79** 134505
[24] Nomura Y, Mizuno T, Kambara H, Nakagawa Y, Watanabe T, Kakeya I and Suzuki M 2014 *J. Phys.: Conf. Ser.* **507** 012038
[25] Nomura Y, Mizuno T, Kambara H, Nakagawa Y and Kakeya I 2015 *J. Phys. Soc. Japan* **84** 013704
[26] Takahashi Y, Kakehi D, Takekoshi S, Ishikawa K, Ayukawa S and Kitano H 2016 *J. Phys. Soc. Japan* **85** 073702
[27] Warburton P A, Saleem S, Fenton J C, Korsah M and Grovenor C R M 2009 *Phys. Rev. Lett.* **103** 217002
[28] Kawabata S, Kashiwaya H and Kashiwaya S 2010 *Physica* C **470** S848–50
[29] Kakeya I, Hamada K, Tachiki T, Watanabe T and Suzuki M 2009 *Supercond. Sci. Technol.* **22** 114014
[30] Martinis J M, Devoret M H and Clarke J 1987 *Phys. Rev.* B **35** 4682–98
[31] Wallraff A, Lukashenko A, Coqui C, Kemp A, Duty T and Ustinov A V 2003 *Rev. Sci. Instrum.* **74** 3740–8
[32] Kubo Y, Takahide Y, Ueda S, Takano Y and Ootuka Y 2010 *Appl. Phys. Express* **3** 063104

[33] Nomura Y, Okamoto R and Kakeya I 2017 *IEEE Trans. Appl. Supercond.* **27** 7200205
[34] Kramers H 1940 *Physica* **7** 284
[35] Caldeira A O and Leggett A J 1981 *Phys. Rev. Lett.* **46** 211
[36] Suzuki M, Ohmaki M, Takemura R, Hamada K, Watanabe T, Ota K, Kitano H and Maeda A 2008 *J. Phys.: Conf. Ser.* **129** 012033
[37] Ota K, Maeda A, Machi T, Tanabe K and Kitano H 2009 *J. Phys.: Conf. Ser.* **150** 052205
[38] Suzuki M, Yamada Y, Kakeya I, Kojima S and Anagawa K 2010 *J. Phys.: Conf. Ser.* **234** 042035
[39] Kitano H, Takahashi Y, Kakehi D, Yamaguchi H, Koizumi S and Ayukawa S 2016 *J. Phys. Soc. Japan* **85** 054703
[40] Kakehi D, Takahashi Y, Yamaguchi H, Koizumi S, Ayukawa S and Kitano H 2016 *IEEE Trans. Appl. Supercond.* **26** 1800204
[41] Kato T and Imada M 1996 *J. Phys. Soc. Japan* **65** 2963
[42] Kubo Y, Sboychakov A O, Nori F, Takahide Y, Ueda S, Tanaka I, Islam A T M N and Takano Y 2012 *Phys. Rev.* B **86** 144532
[43] Koyama T 2016 private communication

Superconductor Science and Technology

PAPER

Engineering and characterization of a packaged high-T_c superconducting terahertz source module

To cite this article: Manabu Tsujimoto *et al* 2017 *Supercond. Sci. Technol.* **30** 064001

IOP Publishing Superconductor Science and Technology
Supercond. Sci. Technol. 30 (2017) 064001 (8pp) https://doi.org/10.1088/1361-6668/aa67aa

Engineering and characterization of a packaged high-T_c superconducting terahertz source module

Manabu Tsujimoto[1,2], Takuji Doi[3], Genki Kuwano[2], Asem Elarabi[3] and Itsuhiro Kakeya[3]

[1] Faculty of Pure and Applied Sciences, University of Tsukuba, 1-1-1 Tennodai, Tsukuba, Ibaraki 305-8573, Japan
[2] Graduate School of Pure and Applied Sciences, University of Tsukuba, 1-1-1 Tennodai, Tsukuba, Ibaraki 305-8573, Japan
[3] Department of Electronic Science and Engineering, Kyoto University, Kyoto-daigaku Katsura, Nishikyo-ku, Kyoto 615-8510, Japan

E-mail: tsujimoto@ims.tsukuba.ac.jp

Received 30 December 2016, revised 11 March 2017
Accepted for publication 20 March 2017
Published 3 May 2017

Abstract

We present an effective engineering technique for compactly packaging high-T_c superconducting continuous-wave terahertz source modules. A terahertz-emitting device, which consists of stacks of intrinsic Josephson junctions in single crystalline $Bi_2Sr_2CaCu_2O_{8+\delta}$, bias electrodes, a collimating lens, and other components, is packaged into a single finger-sized assembly. The rigid and stable structure used for the packaging guarantees physical and chemical stability with good thermal contact, and provides reproducible characteristics with a high yield rate. The coherent terahertz waves can be emitted from the back side of the base crystal without significant screening. The intuitive results obtained from the numerical simulation are consistent with the observed thermal properties. The modules are easy to use, and thus intended for all users unfamiliar with superconducting electronic devices.

Keywords: Bi-2212, intrinsic Josephson junction, terahertz source, packaging module

(Some figures may appear in colour only in the online journal)

1. Introduction

Terahertz (1 (THz) = 10^{12} (Hz)) radiation bridges the gap between the microwave and optical regimes to offer significant scientific and technological potential in many fields [1]. The possibility of compact, solid-state, and continuous-wave (CW) terahertz sources has received extensive attention in the field of semiconductors and lasers, with applications in sensing [2], imaging [3], and spectroscopy [4]. Striking progress has been made in the development of the necessary diode sources: Gunn, IMPATT [5], TUNNETT [6], and resonant tunneling diodes (RTD) [7]. Transistor-based oscillators, for example, the heterojunction bipolar transistor, high electron mobility transistor, and Si-CMOS, have also attracted attention in recent years [8, 9]. Quantum cascade lasers can emit intense radiation at frequencies greater than 1.45 THz, although they must be cooled to 37 K [10]. A RTD oscillator operating at room temperature can generate frequencies up to 1.92 THz [11]; however, a radiation power greater than 1 mW remains out of reach. The required characteristic features of CW terahertz sources are as follows: small in size, easy to use, stable emission, 1 mW power, coherent wave, and broadly tunable.

The observation that coherent terahertz radiation is emitted from a stack of intrinsic Josephson junctions in $Bi_2Sr_2CaCu_2O_{8+\delta}$ (Bi-2212) [12] highlighted the novel possibility of using a high-transition-temperature (high-T_c) superconductor as a convenient terahertz source [13]. The application of a DC voltage V_0 to a stack containing N junctions led to the generation of an AC current and concomitant radiation at the Josephson frequency,

$$f_J = \frac{2e}{h} \cdot \frac{V_0}{N}, \tag{1}$$

where e and h are the elementary charge and Planck's constant, respectively [14]. The maximum output power of 0.6 mW was obtained from arrayed stacks [15], which is presently the highest recorded level among all available sources in this frequency regime, including semiconductor-based devices. The coherence of the emitted waves was established by linewidth measurements using a superconducting integrated receiver [16]. The potential advantage of using high-T_c sources is their broad tunability [17]—the reported broadest tunability extends continuously from 0.5 to 2.4 THz [18]. For comparison, the tunability of a single RTD source is 5% at best [19].

Previous studies have shown that the thermal management of emitting sources is a key requirement for controlling their characteristics [20–34]. Previously, radiation above 1 THz was achieved by an improved cooling technique [27]. Because a local temperature rise in the stack due to the enormous amount of Joule heating was shown to suppress the output power [29], stand-alone type mesas with large effective cooling areas have been studied to determine if they have the potential to generate a 1 mW level of radiation [33, 35]. However, there remains a significant characteristic variation with a low yield rate for the stand-alone type mesas, and they show poor structural and thermal stabilities, which are associated with the complicated fabrication processes. In the present work, we establish an effective engineering technique for packaging the source modules, where an emitting source device, thermal bath, bias electrodes, collimating lens, and other component parts are all included in one packaged assembly. Coherent and tunable CW terahertz radiation can be emitted from the back side of the sapphire substrate to free space via a collimating hemispherical lens. Our packaged modules are easy to use, and thus intended for all users who are unfamiliar with superconducting devices.

2. Experimental setup

The fabrication process of the terahertz-emitting source device is as follows. First, Bi-2212 single crystals grown by a traveling solvent floating zone technique are annealed at 650 °C for 12 h in argon gas. The temperature dependence of the c-axis resistance shows the behavior that is typical of underdoped Bi-2212 with $T_c = 81.3$ (K) (see the inset of figure 3(a) for details). A small piece of the Bi-2212 crystal is glued onto a $7 \times 7 \times 0.3\ \mathrm{mm}^3$ sapphire substrate using low-viscosity cryogenic epoxy resin STYCAST® 1226. A silver electrode layer with a thickness of 0.1 μm is then evaporated onto the surface of the cleaved crystal. A submillimeter-size rectangular mesa structure is milled from the crystal surface by photolithography and argon ion milling techniques. For this particular device, the mesa width was 73 μm and the length was 400 μm. The mesa thickness of 1.1 μm corresponds to $N = 720$. The detailed characteristics are described in our previous paper [29].

Figures 1(a)–(c) show the schematic views and a photograph of the packaged terahertz source module, respectively. The module is small in size at $15 \times 30 \times 5.5\ \mathrm{mm}^3$. This sophisticated finger-size module includes all of the components required to provide superior performance. The emitting device is attached to a copper body using four phosphor-bronze clamps and a small amount of cryogenic high vacuum grease APIEZON® to ensure good thermal contact. A hemispherical collimation lens made of high-resistivity-float-zone (HRFZ) silicon with a radius of $r = 4$ (mm) is held at the aperture position of the copper body using a plastic Teflon supporting plate. After attaching and wiring the emitting device, we then mold the entire assembly by pouring thermally conductive cryogenic epoxy resin STYCAST® 2850 into the cup of the copper body. Figure 2(a) shows the detailed vertical cross-sectional view of the packaged module. An enlarged illustration of the emitting Bi-2212 mesa is shown in figure 2(b). The module is firmly attached to the cold bath with two mounting screws. The distance between the emitting Bi-2212 mesa and the collimation lens is set equal to the focal length, $r/(n-1) = 0.83$ (mm), where $n = 3.41$ is the refractive index of HRFZ silicon. The emitted terahertz waves can penetrate through the underlying Bi-2212 base crystal without significant screening by the excited quasiparticles and superconducting currents.

Some demonstrable advantages of our packaged modules are as follows: the fairly rigid and stable structure guarantees physical and chemical stability with good thermal contact. Therefore, the modules provide stable and reproducible emission characteristics with a high yield rate in contrast to those for stand-alone-type devices. We fabricated two packaged modules to examine the characteristic variation, and they exhibited reproducible current–voltage *(I–V)* and emission characteristics. The modules are as easy to use as conventional semiconducting LED light sources—researchers who are not experienced in using superconducting devices can easily operate them to generate desirable CW terahertz waves. All that is required is the application of a DC voltage to the device via the protruding electrode wires. The module can be mounted to any type of refrigerator and cryocooler system, depending on the intended use. The emitted waves are concentrated into a unidirectional beam by the collimating lens, which provides high efficiency in the use of the emitted electromagnetic energy. In addition, the use of cryogenic epoxy resins in the molding technique allows permanent use without damage from the oxygen and water vapor in air.

Figure 2(c) shows a schematic view of the experimental setup for measuring the *I–V* and emission characteristics. The emitting device was biased using the DC voltage source. During the *I–V* measurements, we also monitored the terahertz-emission power using a silicon composite bolometer with a 1 THz low-pass filter. For detection of the lock-in, the emitted waves were optically chopped at approximately 80 Hz. The output signal was amplified by a high-pass 200× preamplifier and recorded on a computer. The noise

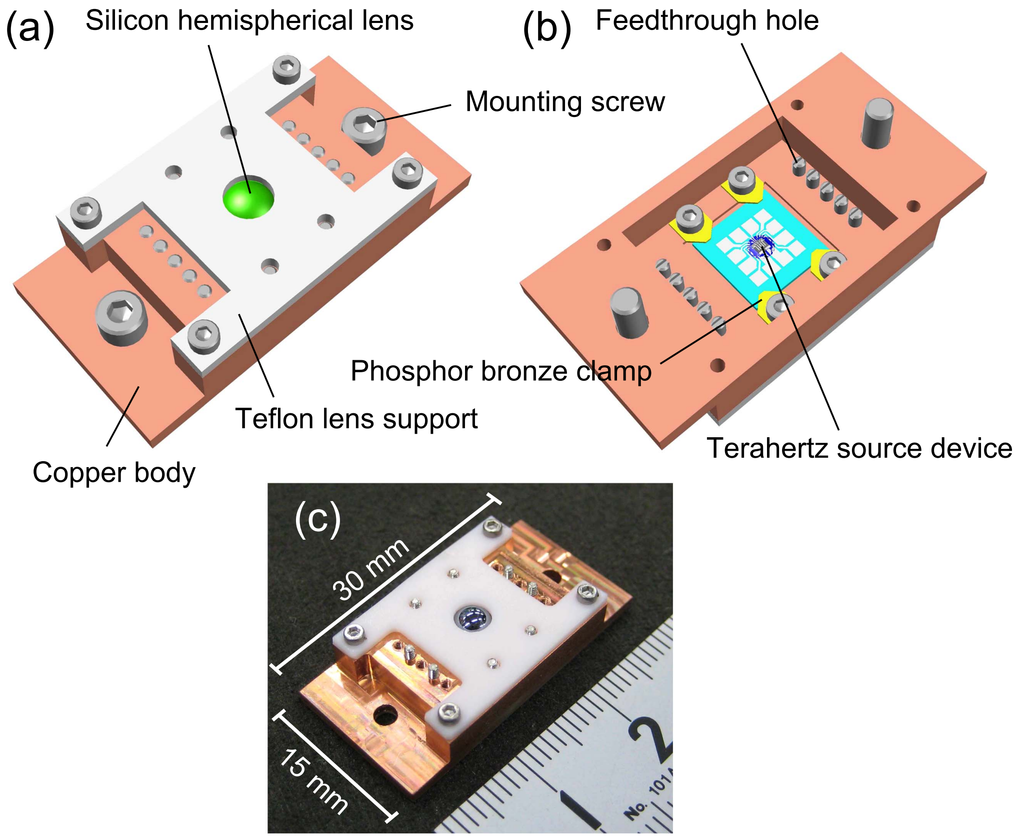

Figure 1. Schematic views of the packaged CW terahertz source module: (a) front view, and (b) back view. (c) Photo of the assembled module.

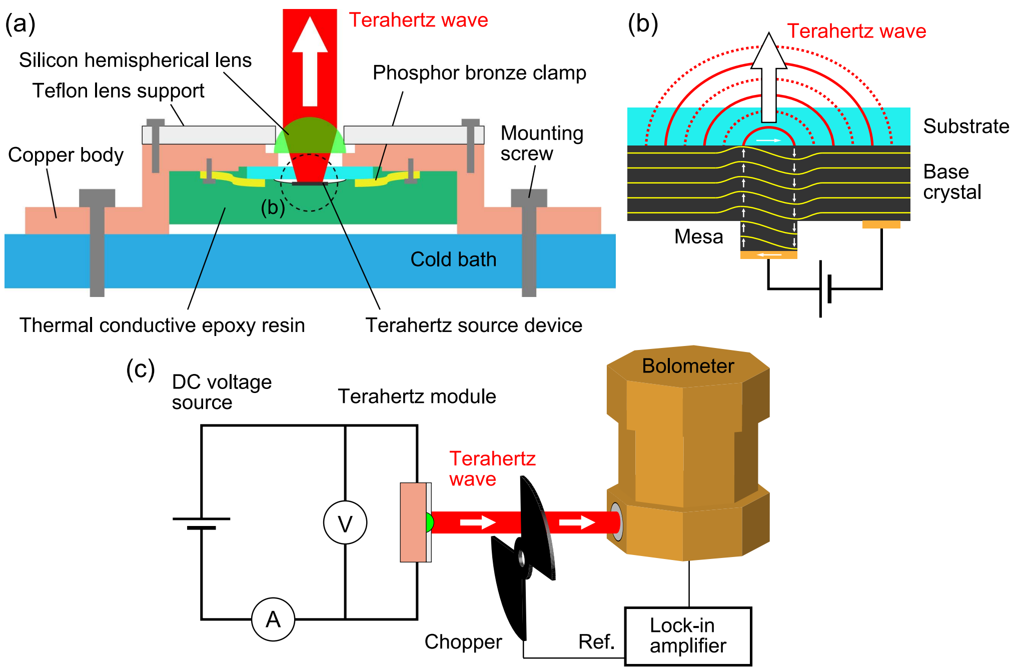

Figure 2. (a) Vertical cross-sectional view of the assembled terahertz source module. CW terahertz waves are emitted from the embedded source device to free space via a silicon hemispherical lens. (b) Enlarged schematic of the terahertz-emitting part encircled in (a). The solid lines represent the standing waves of the *c*-axis electric fields in the Bi-2212 mesa and base crystal associated with the Josephson plasma waves. (c) Schematic view of the experimental setup for *I*–*V* and terahertz-emission characterization.

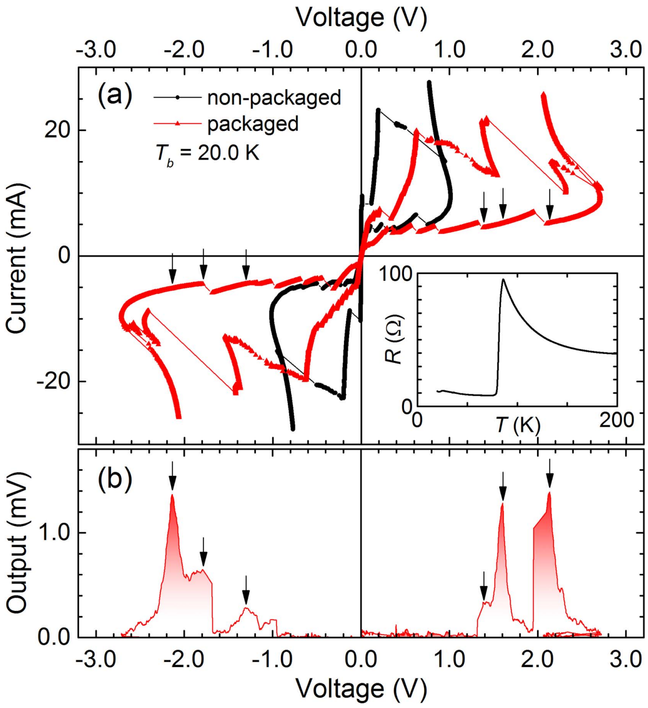

Figure 3. (a) Four-terminal *I*–*V* characteristics measured at $T_b = 20$ (K) for non-packaged (black) and packaged (red) conditions. Inset: temperature dependence of the *c*-axis resistivity. (b) Bolometer output as a function of voltage in the same scale as that of figure 3(a) for the packaged condition.

equivalent power of the detector was 1.4×10^{-13} W Hz$^{-1/2}$. To measure the emission frequency, we used a home-built Fourier transform infrared (FT-IR) spectrometer consisting of a pair of flat lamellar mirrors (not shown here) [36]. The frequency resolution of the spectrometer is given by $\Delta f \sim c/2d_{\max}$, where $d_{\max}$ is the maximum differential displacement of the lamellar mirror and *c* is the speed of light. In the present setup, $d_{\max} = 25$ mm and, therefore, $\Delta f = 6$ GHz. The engineered source module was mounted on a helium-flow cryostat, and the bath temperature T_b was monitored using a thermometer attached to the cold bath. Since the terahertz wave is strongly absorbed by water vapor, it is preferable to use a dry nitrogen box between the cryostat and the bolometer.

3. Results and discussion

Figure 3(a) shows the four-terminal *I*–*V* characteristics measured at $T_b = 20$ (K). The red plot indicates the data when the emitting device was mounted on the module, as shown in figure 2(a). For comparison purposes, the black plot indicates the data when the device was mounted directly on the cold finger of the He-flow cryostat using silver paste as a glue in a conventional manner. When measuring the characterizations, we removed the capping resin used for molding the emitting device in order to separately determine the packaging and aging effects. Each *I*–*V* curve was obtained by a cyclic bias scan. The large hysteresis loop and the multiple branching structures in the low current regime exhibited behaviors typical of the intrinsic Josephson junction system. Since the gap voltage per junction was approximately 20 mV, the present stack with $N = 720$ should provide sufficient hysteresis with the maximum voltage of $N \times 20$ (mV) = 10 (V). Nevertheless, the actual applicable voltage was compressed into the range of 2–3 V. This is attributed to the local temperature rise due to the enormous Joule heating, which gave rise to a decrease in the junction resistance. The strongly negative temperature coefficient of the *c*-axis resistivity (*R*) shown in the inset of figure 3(a) is thought to contribute to hot-spot formation in biased Bi-2212 mesas [24].

Figure 3(b) shows the bolometer output as a function of voltage for the case of the packaged module. Intense terahertz emissions were observed in the low current regime indicated by the arrows in the figure. The module can generate a constant emission power with fluctuations less than a few percent as long as the bias point is fixed. The asymmetric behavior of the bolometer output under positive and negative voltage biases is attributed solely to randomness in the electrical switching during the *I*–*V* scans, which is a trivial issue in the intrinsic Josephson junction system. According to the sensitivity of the bolometer, the output signal of 1 mV corresponds to the emission power of 130 pW. By considering the directivity factor, the integral emission power is estimated to be in the order of microwatts. In the inner *I*–*V* branches where only some of stacked junctions were in the resistive state, the voltage per resistive junction corresponding to the Josephson frequency remained at almost a constant value. The emitted waves were linearly polarized and associated with the transverse magnetic cavity resonance [37, 38], where the *E*-field oscillated along the plane containing the *c*-axis and mesa width.

It is worth mentioning that, to the best of our knowledge, this is the first observation of terahertz radiation emitted from the back side of an underlying large Bi-2212 base crystal. The emission intensity was found to be comparable to that of the front side. It is speculated that the synchronization among adjacent multiple stacks of intrinsic junctions, which leads to significantly high-power radiation, is mediated by the Josephson plasma waves in the base crystal [15, 39]. More importantly, this observation indicates that the oscillating backside surface current associated with the excitation of the Josephson plasma throughout the entire crystal produces the intense radiation, as illustrated in figure 2(b). It is also likely that the emitted waves can penetrate through the base crystal without being screened by the excited quasiparticle current, since the high-T_c superconducting energy is supposed to be higher than the terahertz photon energy. Regardless, the option of backside radiation greatly expands the design possibilities of high-T_c terahertz sources. For example, we now expect to increase the emission intensity by positioning the reflector antenna at the back of the source.

The remarkable change in the hysteretic *I*–*V* loop shown in figure 3(a) provides a strong indication of the improved thermal contact due to the packaging. The thermal equilibrium condition in the resistive state is determined by a delicate balance between the Joule heating that is characterized by the *I*–*V* product and the thermal diffusion. Using our

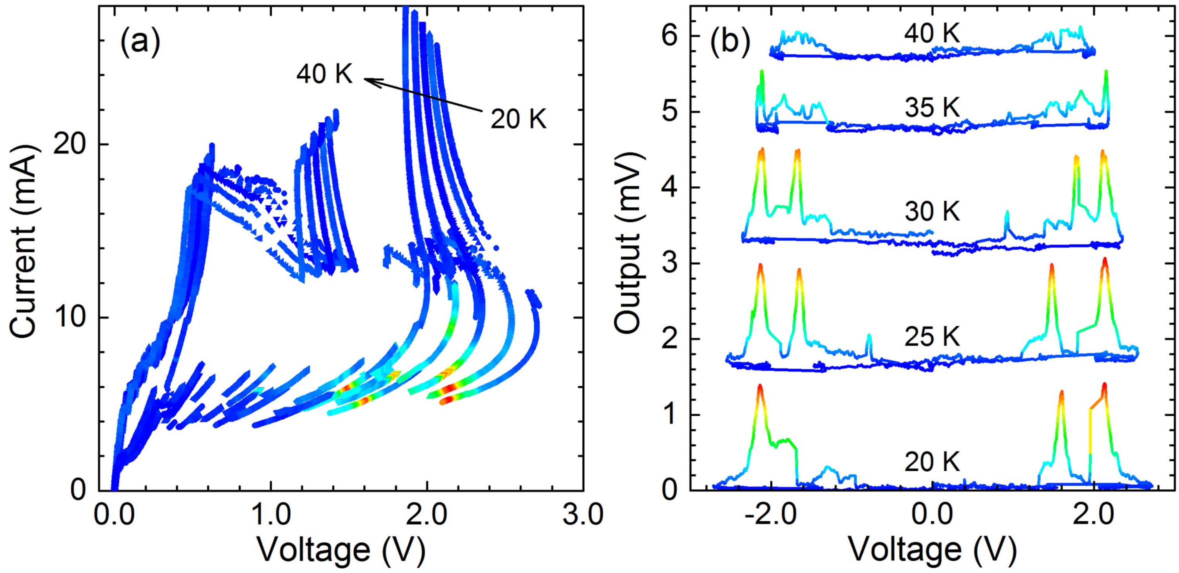

Figure 4. T_b-dependence of the (a) I–V characteristics, and (b) bolometer output. The data are plotted with the color-coded bolometer output.

packaging technique, the excessive temperature rise is suppressed despite the larger I–V product that leads to more severe heating. We presume that this can be attributed to the use of the phosphor-bronze clamps, although epoxy molding is also an effective way to promote sufficient cooling. In fact, if we do not use the clamps, the obtained I–V characteristics and concomitant emission properties were quite sensitive to the amount of silver paste used for gluing.

Figure 4(a) shows the T_b dependence of the I–V characteristics, and T_b varied from 20 to 40 K at 5 K intervals. Based on the negative temperature coefficient of the c-axis superconducting energy gap, the I–V hysteresis decreased as T_b increased. In figure 4(b), the bolometer output at each T_b are plotted with an offset for ease of comparison. In these two panels, the obtained data is plotted with color-coded bolometer output. The maximum output power simply decreased with increasing T_b, and no appreciable emission was detected above $T_b = 40$ (K). This implies that the effective temperature of the biased mesa was close to T_c above $T_b = 40$ (K). We expect that this challenging self-heating problem will be solved by short-pulse techniques [40, 41].

Figure 5 shows the emission spectra measured using the FT-IR spectroscopy. Here, these data were obtained from the packaged module that comes with a 70 μm wide emitting mesa. The distinct spectral peaks are observed at 0.505 THz (0.817 V), 0.522 THz (0.829 V), 0.553 THz (0.885 V), and 0.569 THz (0.894 V), respectively, where the voltage V is indicated on each spectrum. The solid lines represent Lorentzian peak functions with the best fits to the experimental data. The inset of figure 5 shows a linear relationship between V and the central frequency f. The error bars reflect the frequency resolution Δf of the spectrometer. Note that the spectral linewidth associated with the coherence of emitted waves is supposed to be much narrower than Δf [16]. A dashed line in the inset represents the Josephson frequency f_J given by equation (1) with the experimental value of $N = 660$ determined by least-square fits. In this particular case, the f

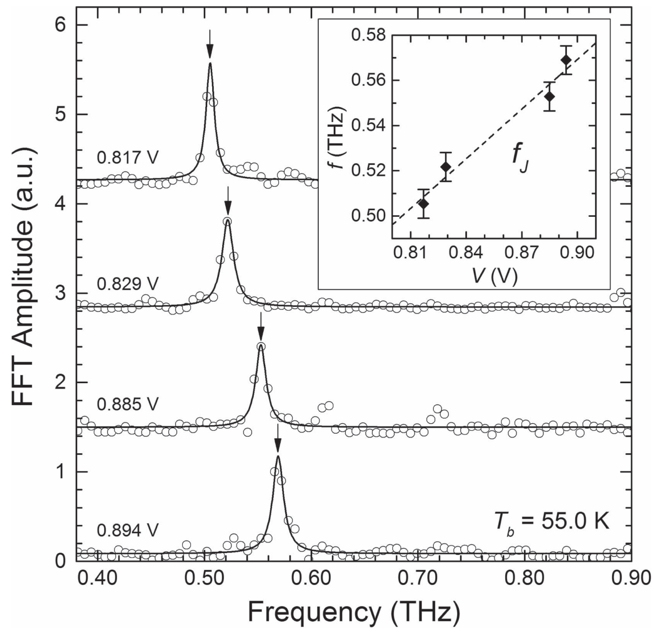

Figure 5. FT-IR emission spectra for a 70 μm wide Bi-2212 mesa. The solid lines represent Lorentzian peak functions with the best fits to the experimental data. Inset: emission frequencies f as a function of V. The error bars reflect the frequency resolution of the spectrometer. A dashed line represents f_J given by equation (1).

tunability of up to 13% was found by varying V. The tunable f range could be extended by examination of the T_b dependence [42] and the inner regions of the branched I–V characteristics [43].

To investigate the effect of the packaging on the thermal properties both quantitatively and qualitatively, we performed a numerical simulation using the COMSOL multiphysics simulation software package (www.comsol.com). By solving the standard equations of electrical and thermal conduction using the 3D finite element method, we can simulate a steady-state temperature distribution in an arbitrary geometry. In

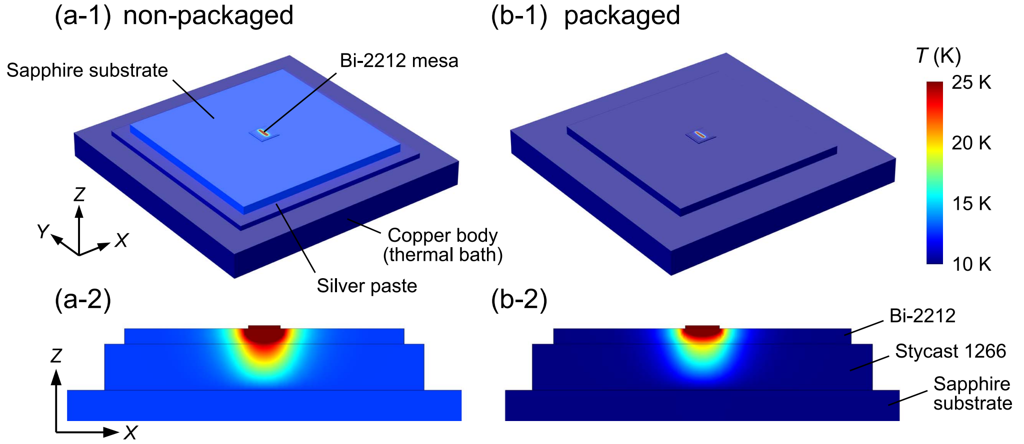

Figure 6. 3D images of the simulated temperature distributions for the (a-1) non-packaged, and (b-1) packaged emitting devices. (a-2) and (b-2) Magnified 2D cross-sectional temperature profiles in the *X–Z* cut plane extracted from the corresponding 3D images.

order to use realistic material parameters, the anisotropic electrical and thermal conductivities of Bi-2212 were extracted from the literature [44]. We also used realistic material parameters available from an extensive materials database, namely, the Network Database System for Thermophysical Property Data (http://tpds.db.aist.go.jp/tpds-web/). Those for STYCAST® 1266 and APIEZON® were found in their respective product data sheets. To make a distinction between the non-packaged and packaged modules, as indicated by the black and red plots in the *I–V* characteristics shown in figure 3(a), we assumed that the emitting device was attached to the copper body in one of two different ways. In the case of the non-packaged device, we used a 0.1 mm thick silver paste as a glue, whereas a small amount of vacuum grease was used in the packaged device.

Figures 6(a-1) and (b-1) show 3D images of the simulated temperature distributions for the non-packaged and packaged cases, respectively. The two panels, namely figures 6(a-2) and (b-2), next to their corresponding 3D images show magnified 2D cross-sectional profiles in the *X–Z* cut plane. A color bar on the right-hand side indicates the temperature scale for each image. We set the bath temperature and bias voltage to 10 K and 2.1 V, respectively, which were extracted from the experimental data shown in figure 3(a). The boundary conditions were chosen to be $dT/dx = 0$ (zero flux) at the lateral and bottom sides of the copper body. For the non-packaged case, the thermal conductivity of silver paste at cryogenic temperatures was set to be 0.4 $\mathrm{W\,m^{-1}\,K^{-1}}$. Importantly, the effective area at the contact boundary between the sapphire substrate and the copper body had to be considered carefully—the real contact area, which is proportional to the heat flux, should have been considerably reduced due to the surface roughness of the silver paste. A surface probe using an atomic force microscope reveals that the actual contact area had decreased by nearly 90% of the apparent area. This was attributed to the relatively large diameter of the thermally conductive silver particles, typically 5 μm. Thus, we began by inserting an interfacial thermal resistance with 10% conductivity on the assumption that the heat transfer would be inhibited at the contact surface.

After repeated simulations, we found that the increase in the effective area at the contact surface was key to the prevention of overheating. The homogeneous temperature distribution over the whole substrate was attributed to the extremely high thermal conductivity of the sapphire. Nevertheless, in the non-packaged case (see figures 6(a-1) and (a-2)), the substrate temperature increased globally by 4 K with respect to T_b due to the deteriorating thermal contact. Furthermore, the maximum local temperature at the emitting Bi-2212 mesa was 35.8 K for the non-packaged case, whereas it was 30.8 K for the packaged case. This intuitive result is consistent with the observed *I–V* characteristics—an emitting device that is attached with a better thermal contact exhibits a larger hysteresis in the *I–V* characteristics in accordance with the negative temperature coefficient of the *c*-axis resistivity. Further, terahertz-frequency electromagnetic simulations could provide valuable information about the maximum emission powers from the module after the great improvements in the thermal properties.

4. Conclusion

In conclusion, we engineered compactly-packaged CW terahertz source modules using intrinsic Josephson junction stacks in high-T_c Bi-2212 single crystals. The modules are small in size, i.e., fingertip size, and exhibit reproducible *I–V* and emission characteristics. The coherent and tunable terahertz waves can be emitted through the collimating lens, which is attached to the back side of the sapphire substrate. A numerical approach to simulate the 3D temperature distribution delivered consistent results. The modules are easy to use, and thus are suitable for practical use in many applications, especially in sensing, imaging, spectroscopy, etc.

Acknowledgments

The authors acknowledge T Kashiwagi, H Minami, K Kadowaki, and S Kawabata for valuable discussions. The Bi-

2212 single crystals were provided by Y Nakagawa. Technical support from Kyoto Shisaku was greatly appreciated. This work was supported by KAKENHI (Grants No. 13J04811, No. 26790032, and No. 26286006), the University of Tsukuba Basic Research Support Program Type B, the Program to Disseminate the Tenure Tracking System at the University of Tsukuba, and the Project for University-Industry Cooperation Strengthening in Tsukuba. We would like to thank Editage (www.editage.jp) for English language editing.

References

[1] Tonouchi M 2007 Cutting-edge terahertz technology *Nat. Photon.* **1** 97–105
[2] Mittleman D 2003 *Sensing with Terahertz Radiation* (*Springer Series in Optical Sciences* vol 85) (Berlin: Springer)
[3] Kawase K, Ogawa Y, Watanabe Y and Inoue H 2003 Non-destructive terahertz imaging of illicit drugs using spectral fingerprints *Opt. Express* **11** 2549–54
[4] Jepsen P U, Cooke D G and Koch M 2011 Terahertz spectroscopy and imaging—modern techniques and applications *Laser Photon. Rev.* **5** 124–66
[5] Eisele H and Kamoua R 2004 Submillimeter-wave InP Gunn devices *IEEE Trans. Microw. Theory Tech.* **52** 2371–8
[6] Nishizawa J, Płotka P, Kurabayashi T and Makabe H 2008 706 GHz GaAs CW fundamental-mode TUNNETT diodes fabricated with molecular layer epitaxy *Phys. Status Solidi* c **5** 2802–4
[7] Brown E R, Soderstrom J R and Parker C D 1991 Oscillations up to 712 GHz in InAs/AlSb resonant-tunneling diodes *Appl. Phys.* **58** 2291–3
[8] Seo M *et al* 2011 InP HBT IC technology for terahertz frequencies: fundamental oscillators up to 0.57 THz *IEEE J. Solid-State Circuits* **46** 2203–14
[9] Momeni O and Afshari E 2011 High power terahertz and millimeter-wave oscillator design: a systematic approach *IEEE J. Solid-State Circuits* **46** 583–97
[10] Kumar S 2011 Recent progress in terahertz quantum cascade lasers *IEEE J. Sel. Top. Quantum Electron.* **17** 38–47
[11] Maekawa T, Kanaya H, Suzuki S and Asada M 2016 Oscillation up to 1.92 THz in resonant tunneling diode by reduced conduction loss *Appl. Phys. Express* **9** 024101
[12] Ozyuzer L *et al* 2007 Emission of coherent THz radiation from superconductors *Science* **318** 1291–3
[13] Welp U, Kadowaki K and Kleiner R 2013 Superconducting emitters of THz radiation *Nat. Photon.* **7** 702–10
[14] Josephson B D 1962 Possible new effects in superconductive tunnelling *Phys. Lett.* **1** 251–3
[15] Benseman T M, Gray K E, Koshelev A E, Kwok W-K, Welp U, Minami H, Kadowaki K and Yamamoto T 2013 Powerful terahertz emission from $Bi_2Sr_2CaCu_2O_{8+\delta}$ mesa arrays *Appl. Phys. Lett.* **103** 022602
[16] Li M *et al* 2012 Linewidth dependence of coherent terahertz emission from $Bi_2Sr_2CaCu_2O_8$ intrinsic Josephson junction stacks in the hot-spot regime *Phys. Rev.* B **86** 060505
[17] Tsujimoto M *et al* 2012 Broadly tunable sub-terahertz emission from internal current–voltage characteristic branches generated from $Bi_2Sr_2CaCu_2O_{8+\delta}$ *Phys. Rev. Lett.* **108** 107006
[18] Kashiwagi T *et al* 2015 A high-Tc intrinsic Josephson junction emitter tunable from 0.5 to 2.4 terahertz *Appl. Phys. Lett.* **107** 082601
[19] Asada M, Suzuki S and Kishimoto N 2008 Resonant tunneling diodes for sub-terahertz and terahertz oscillators *Japan. J. Appl. Phys.* **47** 4375–84
[20] Kurter C, Gray K E, Zasadzinski J F, Ozyuzer L, Koshelev A E, Yamamoto T, Kadowaki K, Kwok W-K, Tachiki M and Welp U 2009 Thermal management in large Bi2212 mesas used for terahertz sources *IEEE Trans. Appl. Supercond.* **19** 428–31
[21] Wang H, Guénon S, Yuan J, Iishi A, Arisawa S, Hatano T, Yamashita T, Koelle D and Kleiner R 2009 Hot spots and waves in $Bi_2Sr_2CaCu_2O_8$ intrinsic Josephson junction stacks: a study by low temperature scanning laser microscopy *Phys. Rev. Lett.* **102** 017006
[22] Yurgens A 2011 Temperature distribution in a large $Bi_2Sr_2CaCu_2O_{8+\delta}$ mesa *Phys. Rev.* B **83** 184501
[23] Asai H, Tachiki M and Kadowaki K 2012 Three-dimensional numerical analysis of terahertz radiation emitted from intrinsic Josephson junctions with hot spots *Phys. Rev.* B **85** 064521
[24] Gross B *et al* 2012 Hot-spot formation in stacks of intrinsic Josephson junctions in $Bi_2Sr_2CaCu_2O_8$ *Phys. Rev.* B **86** 094524
[25] Kakeya I, Omukai Y, Yamamoto T, Kadowaki K and Suzuki M 2012 Effect of thermal inhomogeneity for terahertz radiation from intrinsic Josephson junction stacks of $Bi_2Sr_2CaCu_2O_{8+\delta}$ *Appl. Phys. Lett.* **100** 242603
[26] Gross B *et al* 2013 Modeling the linewidth dependence of coherent terahertz emission from intrinsic Josephson junction stacks in the hot-spot regime *Phys. Rev.* B **88** 014524
[27] Ji M *et al* 2014 $Bi_2Sr_2CaCu_2O_8$ intrinsic Josephson junction stacks with improved cooling: coherent emission above 1 THz *Appl. Phys. Lett.* **105** 122602
[28] Minami H, Watanabe C, Sato K, Sekimoto S, Yamamoto T, Kashiwagi T, Klemm R A and Kadowaki K 2014 Local SiC photoluminescence evidence of hot spot formation and sub-THz coherent emission from a rectangular $Bi_2Sr_2CaCu_2O_{8+\delta}$ mesa *Phys. Rev.* B **89** 054503
[29] Tsujimoto M, Kambara H, Maeda Y, Yoshioka Y, Nakagawa Y and Kakeya I 2014 Dynamic control of temperature distributions in stacks of intrinsic Josephson junctions in $Bi_2Sr_2CaCu_2O_{8+\delta}$ for intense terahertz radiation *Phys. Rev. Appl.* **2** 044016
[30] Gross B *et al* 2015 Electrothermal behavior and terahertz emission properties of a planar array of two $Bi_2Sr_2CaCu_2O_{8+\delta}$ intrinsic Josephson junction stacks *Supercond. Sci. Technol.* **28** 055004
[31] Zhou X J *et al* 2015 Tuning the terahertz emission power of an intrinsic Josephson-junction stack with a focused laser beam *Phys. Rev. Appl.* **3** 1–6
[32] Benseman T M *et al* 2015 Current filamentation in large $Bi_2Sr_2CaCu_2O_{8+\delta}$ mesa devices observed via luminescent and scanning laser thermal microscopy *Phys. Rev. Appl.* **3** 044017
[33] Zhou X *et al* 2015 Three-terminal stand-alone superconducting terahertz emitter *Appl. Phys. Lett.* **107** 122602
[34] Kashiwagi T *et al* 2015 Efficient fabrication of intrinsic-Josephson-junction terahertz oscillators with greatly reduced self-heating effects *Phys. Rev. Appl.* **4** 054018
[35] Kitamura T *et al* 2014 Broadly tunable, high-power terahertz radiation up to 73 K from a stand-alone $Bi_2Sr_2CaCu_2O_{8+\delta}$ mesa *Appl. Phys. Lett.* **105** 202603
[36] Eisele H, Naftaly M and Fletcher J R 2007 A simple interferometer for the characterization of sources at terahertz frequencies *Meas. Sci. Technol.* **18** 2623–8
[37] Tsujimoto M, Yamaki K, Deguchi K, Yamamoto T, Kashiwagi T, Minami H, Tachiki M, Kadowaki K and Klemm R A 2010 Geometrical resonance conditions for THz radiation from the intrinsic Josephson junctions in $Bi_2Sr_2CaCu_2O_{8+\delta}$ *Phys. Rev. Lett.* **105** 037005

[38] Tsujimoto M, Kakeya I, Kashiwagi T, Minami H and Kadowaki K 2016 Cavity mode identification for coherent terahertz emission from high-Tc superconductors *Opt. Express* **24** 4591
[39] Lin S Z and Koshelev A E 2013 Synchronization of Josephson oscillations in a mesa array of $Bi_2Sr_2CaCu_2O_{8+\delta}$ through the Josephson plasma waves in the base crystal *Physica* C **491** 24–29
[40] Yasuda T, Tonouchi M and Takano S 1997 Influence of self-heating on the *I–V* characteristics in Bi-2212 intrinsic junctions *Physica* C **289** 109–13
[41] Fenton J C, Thomas P J, Yang G and Gough C E 2002 System for fast time-resolved measurements of *c*-axis quasiparticle conductivity in intrinsic Josephson junctions of $Bi_2Sr_2CaCu_2O_{8+\delta}$ *Appl. Phys. Lett.* **80** 2535
[42] Benseman T M, Koshelev A E, Gray K E and Kwok W K 2011 Tunable terahertz emission from $Bi_2Sr_2CaCu_2O_{8+\delta}$ mesa devices *Phys. Rev.* B **84** 064523
[43] Tsujimoto M, Minami H, Delfanazari K, Sawamura M, Nakayama R, Kitamura T, Yamamoto T, Kashiwagi T, Hattori T and Kadowaki K 2012 Terahertz imaging system using high-Tc superconducting oscillation devices *J. Appl. Phys.* **111** 123111
[44] Crommie M and Zettl A 1991 Thermal-conductivity anisotropy of single-crystal $Bi_2Sr_2CaCu_2O_8$ *Phys. Rev.* B **43** 408–12

Dynamics of First and Second Switches in $Bi_2Sr_2CaCu_2O_{8+\delta}$ Intrinsic Josephson Junction Stacks Measured by Specifically Designed Electronics

Yoshiki Nomura, Riku Okamoto, and Itsuhiro Kakeya

(Invited Paper)

***Abstract*—We measure switching probability distributions for the first and the second switches of stacks of $Bi_2Sr_2CaCu_2O_{8+\delta}$ intrinsic Josephson junctions. To measure switching probability distributions, we design a current source and introduced a microcontroller. The resolution and accuracy are sufficient for measuring switching probability distributions of intrinsic Josephson junctions. For the first switch, crossover temperatures between thermally activated escape and macroscopic quantum tunneling are in the range between 0.8 and 2.2 K. The crossover temperatures of the second switch are approximately 8.0 and 6.8 K for the samples with critical densities of 1.0 and 2.0 kA/cm^2, respectively. We analyze critical current density dependence of the crossover temperature of the second switch. The crossover temperature decreases with increasing critical current density. This anticorrelation can be explained neither by the single-junction model nor by the heating effect. The anticorrelation is a peculiar phenomenon observed in the second switch. We consider that the anticorrelation is attributed to the capacitive coupling. The strength of the capacitive coupling is weaker in IJJs with higher critical current density because the charge screening length is shorter due to increase of carrier density.**

***Index Terms*—High-temperature superconductors, josephson junction, josephson effect, macroscopic quantum tunneling.**

I. Introduction

In intrinsic Josephson junctions (IJJs) included in $Bi_2Sr_2Ca_{n-1}Cu_nO_{4+2+\delta}$ (BSCCO) materials [1], [2], strong coupling effects due to thin superconducting layers are suggested [3], [4]. The capacitive coupling is caused by breaking of the charge neutrality within CuO_2 superconducting layers. The switching dynamics of stacked IJJs is an essential phenomenon to study the coupling between IJJs since switching from the superconducting to the resistive state of IJJ can be resolved in current-voltage ($I-V$) characteristics of the stack.

A current-biased single Josephson junction can be well described by the RCSJ (resistively and capacitively shunted junction) model. In this model, an $I-V$ characteristic of an IJJ is described by a motion of a particle in a tilted washboard potential. The switching from the superconducting state to the resistive state corresponds to the escape of the particle from the potential minima. The escape is induced by either thermal fluctuation or quantum fluctuation. The former and the latter are called as thermally activated escape (TAE) and macroscopic quantum tunneling (MQT). At high temperature, TAE is dominant. Thermal fluctuation become weaker with decreasing temperature and MQT is observed at low temperatures. The temperature where MQT and TAE is equivalent is called as the crossover temperature (T^*).

Recently, intriguing phenomena on MQT have been reported. Crossover temperature of the second switch (T_2^*) is strongly enhanced in the stack of $Bi_2Sr_2CaCu_2O_{8+\delta}$ (Bi2212) [5]–[7]. Note that the first switches changes the number of resistive IJJs in the stack from zero to one and the second switch changes that from one to two. This phenomenon is also observed in $Bi_2Sr_2CuO_{6+\delta}$ (Bi2201) [8]. On the other hand in $Bi_2Sr_2Ca_2Cu_3O_{10+\delta}$(Bi2223), T_2^* is almost identical with that of the first switch [7]. The difference between Bi2212 (Bi2201) and Bi2223 is the thickness of the superconducting CuO_2 layers. Thus the enhancement of T_2^* was found in IJJs with superconducting layers thinner than 0.3 nm. Since the capacitive coupling is attributed to the charge screening length within the CuO_2 layers, such a significant change within a very small change in the thickness of the CuO_2 layers is attributed to the capacitive coupling effect. In Bi2223, $T_2^*$of the second switch is not enhanced since the capacitive coupling is diminished by the thick CuO_2 layer.

In this study, we measure switching probability distributions (SPDs) of the first and second switches in Bi2212. Crossover temperature of the first switch (T_1^*) is approximately 1 K. The SPD of the first switch can be well described by the single junction model. This result is consistent with the previous reports [6], [9]–[12]. On the other hand, T_2^* is much higher than that of the first switch and in the range from 6.8 K to 8.0 K. These results are consistent with the previous reports in Bi2212 [5]–[7]. We analyzed SPDs of the second switch with respect to fluctuation-free critical current density (J_c^0). T_2^* decreases with increasing in J_c^0. This relation cannot be explained by the single junction model. The specific phenomena observed in the second switch are inherently attributed to the interaction between stacked IJJs.

Manuscript received September 6, 2016; accepted December 4, 2016. Date of publication December 20, 2016; date of current version January 20, 2017. This work was supported in part by the JSPS KAKENHI under Grant 16J11491.

The authors are with the Department of Electronic Science and Engineering, Kyoto University, Kyoto 615-8510, Japan (e-mail: nomura@sk.kuee.kyoto-u.ac.jp; okamoto@sk.kuee.kyoto-u.ac.jp; kakeya@kuee.kyoto-u.ac.jp).

Color versions of one or more of the figures in this paper are available online at http://ieeexplore.ieee.org.

Digital Object Identifier 10.1109/TASC.2016.2642043

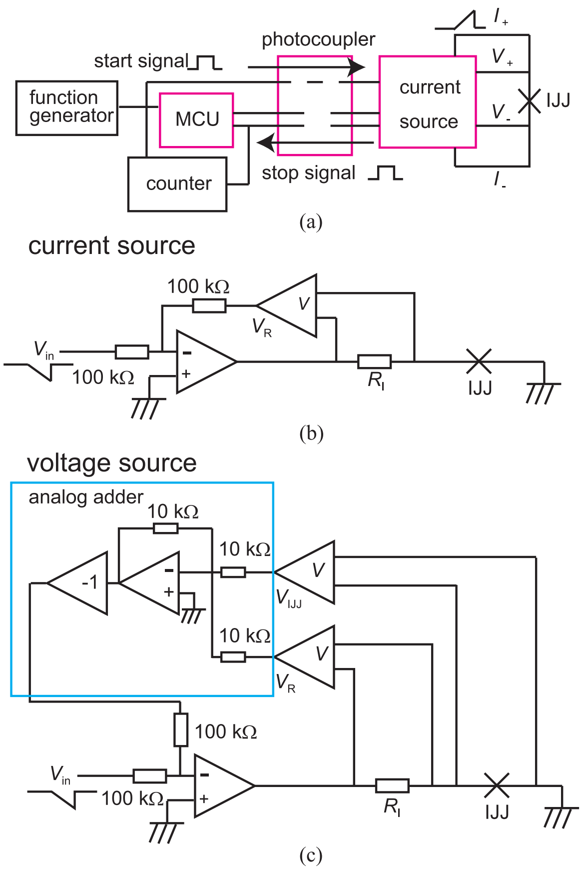

Fig. 1. (a) Schematic of SPD measurement system. Newly introduced devices are indicated by red content. The circuit is operated in (b) a current source and (c) a voltage source.

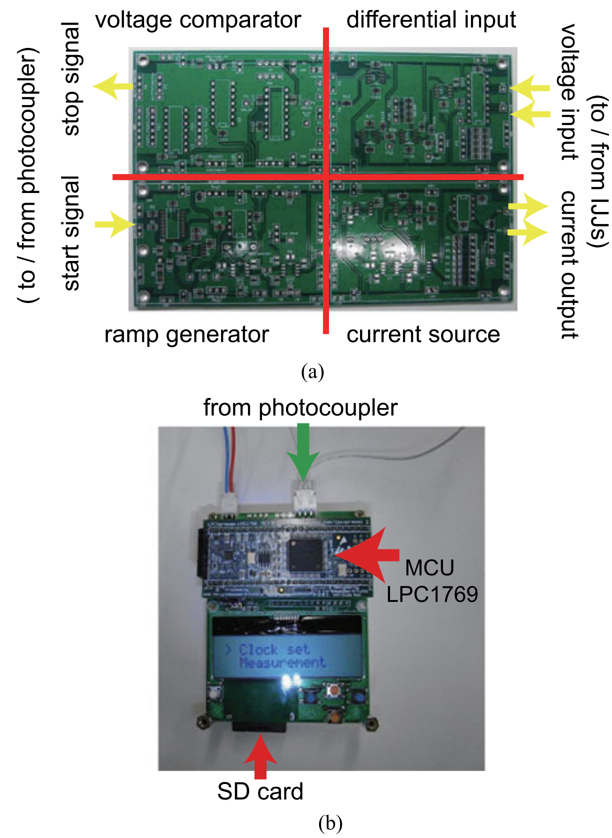

Fig. 2. (a) The printed circuit board of current source. The board is composed of 4 parts divided in red line. Yellow arrows shows the flow of the data or current. (b) The picture of the micro controller (LPC1769). The LPC1769 is operated as the counter. The measured data was saved in the SD card.

The capacitive coupling is one of the candidates to explain the negative correlation because the capacitive coupling is weaker for an IJJ with higher J_c^0. We consider that the capacitive coupling is dominant in the MQT of the second switch.

II. Experimental Method

A Bi2212 single crystal was grown by the traveling solvent floating zone method. The nominal composition is $Bi_{2.15}Sr_{1.85}CaCu_2O_{8+\delta}$. We fabricated mesa structures with in-plane size of $1 \times 1\ \mu m^2$ on the surface of the single crystal by electron-beam lithography and Ar-ion milling method. The details are described in [13]. We describe results in four IJJ stacks with different critical current densities, which are refereed as samples A, B, C, and D. It is considered that the difference of the critical current between sample A and D is due to the slight change of chemical composition between the mesa. Note that the samples used in this experiment are fabricated on the same crystal simultaneously. The structure of the junctions are almost identical. The identical structure is suitable for comparing the characteristics of the Bi2212 IJJs.

SPDs are measured by a time-of-flight method. Fig. 1(a) shows a schematic diagram of the measurement system. In this method, we measure the time from starting bias to switching to the resistive state as follows. First, a start signal is sent from the function generator to the counter and the current source, then a ramp current flows to the IJJs. A stop signal is sent when the voltage in IJJ exceeds a reference voltage. The reference voltage is set to approximately half the gap voltage. The counter measures the elapsed time from the start signal to the stop signal. We can calculate the switching current by multiplying the measured time and the ramp rate of the bias current.

In this study, we used a laboratory-made current source designed for this specific purpose. The current source was made on a printed circuit board (PCB). The Gerber data of the PCB was designed by using KiCad. We combined the current source and a micro controller unit (MCU). The PCB consists of 4 parts as seen in Fig. 2(a). The ramp generator sends a ramp wave immediately after receiving the start signal. The voltage controlled current source applies current to a sample according to the ramp signal. Induced voltage of the sample is monitored by the differential input. The voltage of the IJJ sample is compared with the reference voltage in the voltage comparator. The stop signal is sent by the voltage comparator when the input voltage exceeds the reference voltage. The main circuit is described in elsewhere [14]. We added following three functions to the original circuit. First, two reference voltages can be programmed to measure the first switch and the second switch simultaneously (within a single ramping). Two signals corresponding to the first switch and the second switch are generated by the new system. Second, we can select either a constant current source

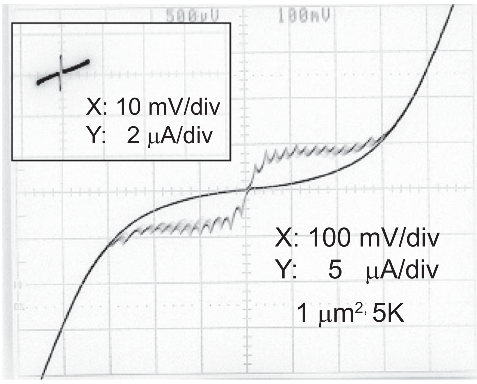

Fig. 3. The $I-V$ characteristic of sample A at 5 K. Inset: The first switch observed under the low bias voltage.

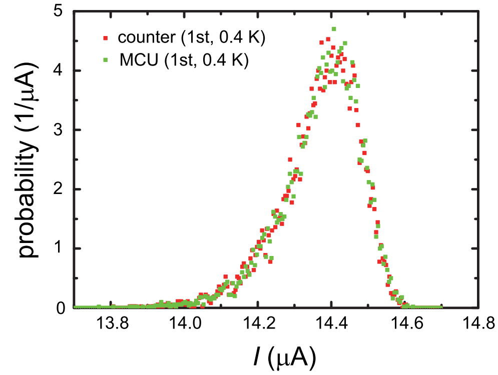

Fig. 4. The SPD at 0.4 K. Red points show the data measured by the calibrated counter. Green points show the data of the MCU counter.

or a constant voltage source as a bias source. The schematics of the current source and voltage source are described in Fig. 1(b) and (c) respectively. An Op-Amp generate the current to IJJs in this circuit. When the circuit operates as the current source ([see Fig. 1(b)], the bias current ($I_{\rm bias}$) is determined as $I_{\rm bias} = -V_{\rm in}/R_{\rm I}$, where $V_{\rm in}$ is the input voltage and $R_{\rm I}$ is a resistance serially inserted to the output of the Op-Amp. $I_{\rm bias}$ is independent of the external impedance including IJJs. When the circuit operate as the voltage source [see Fig. 1(c)], $I_{\rm bias}$ is determined as $I_{\rm bias} = -(V_{\rm in} - V_{\rm IJJ})/R_{\rm I}$, where $V_{\rm IJJ}$ is the voltage of IJJs. When the IJJ is switched to the voltage state, $I_{\rm bias}$ decrease because of increase in the $V_{\rm IJJ}$. The current source and the voltage source can be switched easily by a toggle switch. In this study, we used this as the current source to measure SPDs. Finally, photocouplers (TLP2361) were used for the input and output of the trigger signal to electrically isolate the analog circuit from digital circuit. The electrical noise from the digital instruments is significantly suppressed by this isolation.

Fig. 2(b) shows the MCU counter system. We use an LPC1769 as the MCU which is connected to photocouplers and an SD card directly. Serial Peripheral Interface (SPI) is used for the communication between the MCU and the SD card. The MCU is operated as follows. When the start signal is received, the internal counter starts to measure. When either the first or the second switch takes place, the counter value is copied to an internal register. The counter stops and resets after the signal corresponding to the second switch receiving. Finally, the measured value is written to the SD card. The clock frequency of the counter is 50 MHz corresponding to the time-resolution of 0.02 μsec. This means that the switching current resolution is more accurate than $\sim 10^{-4}$ of the maximum ramped current $\sim 10\,\mu$A because the measured time is usually $\sim 10^{-3}$ sec. We checked its resolution and accuracy by comparing SPDs measured by this and an external calibrated counter, Pendulum CNT-81, used in our previous studies.

III. Results and Discussion

Fig. 3 shows an $I-V$ curve of sample A at 5 K. The number of IJJs included in the sample is 13. The switching current is apparently different between the first switch and the second switch. The switching current of the first switch is 1 μA and that of the second switch is 3 μA. The reduced switching current of the first switch is commonly found in mesa type IJJ stacks because the topmost Ag metal leads to the suppression of the superconductivity of the topmost CuO_2 layers. Thus, we easily distinguish the first switch and second switch because of the large difference in the switching current. The suppression of switching current is an advantage for measurement of SPDs.

Before measuring SPDs at various temperatures, we checked the new measurement system, which consists of the PCB current source and the MCU counter. Fig. 4 shows the SPDs of the first switch at 0.4 K measured by the calibrated counter (red points) and the data measured by the MCU counter (green points). The data look identical. This result shows that the resolution and the accuracy of the MCU is sufficient for our measurement.

Fig. 5 shows SPDs of the first and second switches in sample A. The SPDs are almost identical below 0.53 K for the first switch. The distribution width becomes broader and switching current becomes smaller with increasing temperature above 0.53 K. The distribution width becomes narrower again above 2.3 K. For the second switch, temperature dependence of the SPD is qualitatively similar to that of the first switch. The distribution width is almost constant below 2.3 K and becomes broader with increasing temperature above 2.3 K. To clarify the temperature dependence of the SPD quantitatively, we calculate effective temperature ($T_{\rm eff}$) by fitting the Kramers formula [15] to the experimental data. The Kramers formula is described by $\Gamma_{\rm TA} = \omega_p/2\pi \exp(-\Delta U/k_B T)$, where $\Gamma_{\rm TA}$ is escape rate of thermal activation, ω_p is Josephson plasma frequency, ΔU is potential barrier in the tilted washboard potential and k_B is the Boltzmann constant. The relation between SPD (P) and escape rate (Γ) is $P = \Gamma(dI/dt)^{-1}(1 - \int P(u)du)$, where dI/dt is the ramp ratio which is described in Table I. Fig. 6 shows the plot of $T_{\rm eff}$ as a function of bath temperature $T_{\rm bath}$. We plotted the results of sample A and D. In sample A, $T_{\rm eff}$ for the first switch is temperature independent below 0.8 K, is almost equal to $T_{\rm bath}$ between 0.8 K and 2.3 K, and then becomes smaller than $T_{\rm bath}$ due to the phase diffusion above 2.3 K. In sample D, the temperature dependence of $T_{\rm eff}$ is similar to sample A. $T_{\rm eff}$ is temperature independent below 1.2 K and is equal to $T_{\rm bath}$ above 2.0 K. T_1^* is estimated as 0.86 and 1.2 K in sample A and D, respectively. This temperature dependence is well described

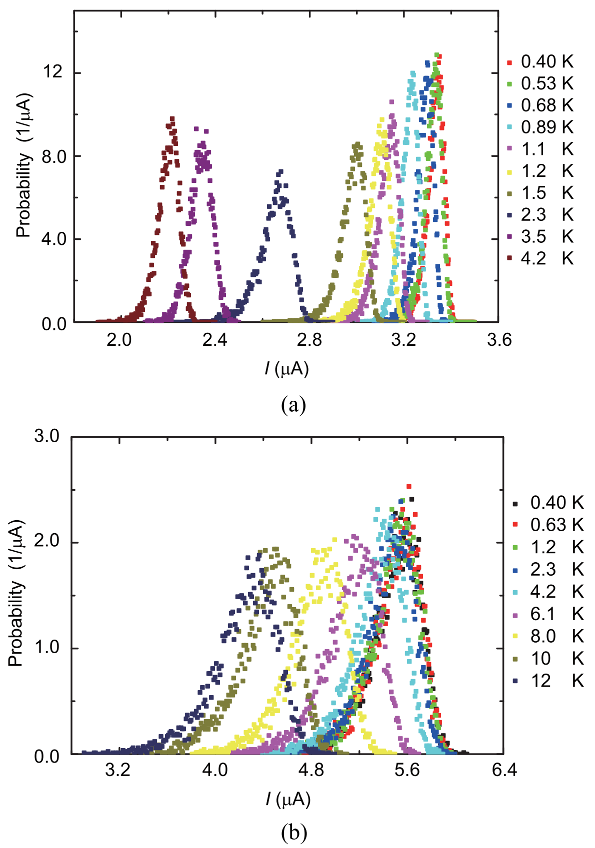

Fig. 5. (a) SPDs of the first switch in sample A. (b) SPDs of the second switch in sample A.

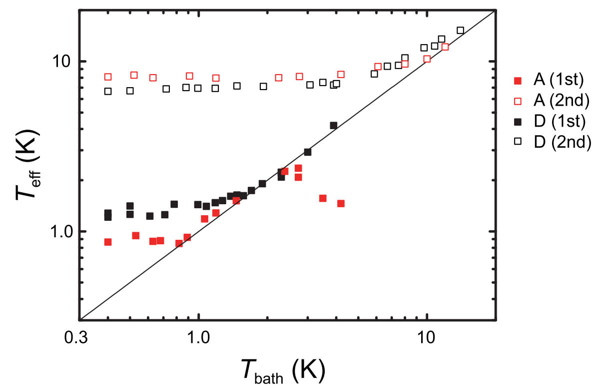

Fig. 6. The plot of the $T_{\rm eff}$ versus $T_{\rm bath}$. Red points show the data of sample A. Black points show the data of sample D.

TABLE I
CHARACTERISTICS OF THE FOUR SAMPLES

sample	A	B	C	D
dI/dt (A/sec)	8.0×10^{-4}	2.5×10^{-3}	2.6×10^{-3}	2.3×10^{-3}
J^0_{c1} (kA/cm^2)	0.40	0.69	0.86	0.46
T^*_1 (K)	0.86	2.2	1.4	1.2
J^0_{c2} (kA/cm^2)	1.0	1.4	1.8	1.9
T^*_2 (K)	8.1	7.4	6.8	6.7

by the single junction model as well as previous reports [9]. In contrast, T^*_2 is quite different from T^*_1. T^*_2 is estimated 8.0 and 6.8 K in sample A and D, respectively. T^*_2 is much higher than that of first switch in both sample A and D. Table I lists obtained parameters of sample A to D. J^0_{c1} is fluctuation-free critical current of the first switch and J^0_{c2} is that of the second switch. Obviously, T^*_2 is higher than T^*_1 in all samples. The enhancement of T^*_2 is observed regardless of the difference in switching current densities of the second switch.

We note that temperature rise of the stack due to self-heating cannot be negligible in case of the second switch. In sample A, $T_{\rm eff}$ corresponds to $T_{\rm bath}$ above 10 K. However, in sample D, $T_{\rm eff}$ is 1 K higher than $T_{\rm bath}$ above 10 K in spite of lower T^*_2. We consider that the offset was observed due to the heating effect. The bias voltage at the first branch (before the second switch) is about 20 mV as seen in Fig. 3. The heat quantity calculated by $I * V$ is not zero in the second switch. As a result, temperature of IJJ is possibly higher than $T_{\rm bath}$. This is the main reason for the slightly upward shift of $T_{\rm eff}$. Although the heating effect cannot be negligible, the heating effect is not dominant for the enhancement of T^*_2. The offset due to the heating effect is about 1 K which is substantially smaller than $T^*_2 \sim 6$ K. The inductive coupling due to the Josephson vortices (fluxons) has previously been investigate. The SPD becomes broad and has multiple peaks by fluxons [16], [17]. In this study, the multiple peaks is not observed in sample A to D. We consider that the coupling due to the fluxon is negligible in this experiment using small size mesa structure.

Next, we discuss the evolution of T^*_2 as a function of J^0_{c2}. The sets of data (J^0_{c2}, T^*_2) in samples A to D are listed in Table I. T^*_2 decrease with increasing J^0_{c2}. This anti-correlation cannot be explained by the single junction model. In single junction model, the T^* is proportional to the square root of the J^0_c, which has a positive correlation. The anti-correlation with J^0_{c2} is an unique phenomenon observed in the second switch. The anti-correlation can be explained by the capacitive coupling. The capacitive coupling become weak with increasing the J^0_{c2} since the charge screening length become short. As a result, the enhancement of the second switch is suppressed.

IV. CONCLUSION

We measured SPDs of the first and second switch in the stacks of the Bi2212. To measure the first and second switch simultaneously, we built the new SPD measurement system. The resolution and accuracy are sufficient for measuring SPDs of IJJs. The SPDs of the first switch are well described by the single junction model. T^*_2 is enhanced compared with that of the first switch. Moreover, T^*_2 decrease with increase in J^0_{c2}. This anti-correlation cannot be explained by the single junction model. We consider that the anti-correlation can be explained by the relation between the strength of the capacitive coupling and J^0_c.

ACKNOWLEDGMENT

The authors would like to thank O. Sakai at University of Shiga Prefecture for allowing them to use the electron-beam lithography.

REFERENCES

[1] R. Kleiner, F. Steinmeyer, G. Kunkel, and P. Müller, "Intrinsic Josephson effects in $Bi_2Sr_2CaCu_2O_8$ single crystals," *Phys. Rev. Lett.*, vol. 68, pp. 2394–2397, 1992.

[2] R. Kleiner and P. Müller, "Intrinsic Josephson effects in high-T_c superconductors," *Phys. Rev. B*, vol. 49, pp. 1327–1341, 1994.

[3] T. Koyama and M. Tachiki, "I–V characteristics of Josephson-coupled layered superconductors with longitudinal plasma excitations," *Phys. Rev. B*, vol. 54, pp. 16183–16191, 1996.

[4] S. Sakai, P. Bodin, and N. F. Pederson, "Fluxons in thin-film superconductor-insulator superlattices," *J. Appl. Phys.*, vol. 73, pp. 2411–2418, 1991.

[5] H. Kashiwaya *et al.*, "Switching Dynamics of $Bi_2Sr_2CaCu_2O_{8+\delta}$ Intrinsic Josephson Junctions: Macroscopic Quantum Tunneling and Self-Heating Effect," *Phys. Soc. Jpn.*, vol. 77, no. 10, 2008, Art. no. 104708.

[6] K. Ota *et al.*, "Comparative study of macroscopic quantum tunneling in $Bi_2Sr_2CaCu_2O_y$ intrinsic Josephson junctions with different device structures," *Phys. Rev. B*, vol. 79, no. 13, 2009, Art. no. 134505.

[7] Y. Nomura *et al.*, "Systematic enhancements of switching rate in intrinsic Josephson junctions," *J. Phys.: Conf. Ser.*, vol. 507, 2014, Art. no. 012038.

[8] Y. Nomura, T. Mizuno, H. Kambara, Y. Nakagawa, and I. Kakeya, "Enhanced macroscopic quantum tunneling in capacitively coupled BiPb2201 single-layered intrinsic Josephson junctions," *J. Phys. Soc. Jpn.*, vol. 84, no. 1, 2015, Art. no. 013704.

[9] K. Inomata *et al.*, "Macroscopic quantum tunneling in a *d*-wave high-T_c $Bi_2Sr_2CaCu_2O_{\delta+8}$ superconductor," *Phys. Rev. Lett.*, vol. 95, no. 10, 2005, Art. no. 107005.

[10] X. Y. Jin, J. Lisenfeld, Y. Koval, A. Lukashenko, A. V. Ustinov, and P. Muller, "Enhanced macroscopic quantum tunneling in $Bi_2Sr_2CaCu_2O_{8+\delta}$ intrinsic Josephson-junction stacks," *Phys. Rev. Lett.*, vol. 98, no. 17, 2006, Art. no. 177003.

[11] S. X. Li *et al.*, "Observation of macroscopic quantum tunneling in a single $Bi_2Sr_2CaCu_2O_{8+\delta}$ surface intrinsic Josephson junction," *Phys. Rev. Lett.*, vol. 99, 2007, Art. no. 037002.

[12] H. Kashiwaya *et al.*, "Multi-Junction Switching in $Bi_2Sr_{1.6}La_{0.4}CuO_{6+\delta}$ Intrinsic Josephson Junctions," *Appl. Phys. Express*, vol. 3, 2010, Art. no. 043101.

[13] I. Kakeya, K. Hamada, T. Tachiki, T. Watanabe, and M. Suzuki, "Switching current distributions and macroscopic quantum tunneling in over-doped BSCCO mesas with nanometer thickness," *Supercond. Sci. Technol.*, vol. 22, 2009, Art. no. 114014.

[14] Y. Kubo, T. Yamaguchi, S. Ueda, Y. Takano, and Y. Ootuka, "Macroscopic quantum tunneling in a $Bi_2Sr_2CaCu_2O_{8+\delta}$ single crystalline whisker," *Appl. Phys. Express*, vol. 3, 2010, Art. no. 063104.

[15] H. Kramers, "Brownian motion in a field of force and the diffusion model of chemical reactions," *Physica*, vol. 7, pp. 284–304, 1940.

[16] N. Mros, V. M. Krasnov, A. Yurgens, D. Winkler, and T. Claeson, "Multiple-valued *c*-axis critical current and phase locking in $Bi_2Sr_2CaCu_2O_{8+\delta}$ single crystals," *Phys. Rev. B*, vol. 57, R8135–R8138, 1998.

[17] V. M. Krasnov, V. A. Oboznov, V. V. Ryazanov, N. Mros, A. Yurgens, and D. Winkler, "Comparison of Josephson fluxon modes in high- and low-temperature superconducting stacked Josephson junctions," *Phys. Rev. B*, vol. 61, pp. 766–777, 2000.

ED3-5

Generation of Circularly Polarized THz Radiation from $Bi_2Sr_2CaCu_2O_{8+\delta}$ Mesa Structures

*Asem Elarabi[1,2], Yusuke Yoshioka[1], Manabu Tsujimoto[2], Itsuhiro Kakeya[1]

Kyoto University[1]
University of Tsukuba[2]

In the last decade, continuous wave terahertz sources based on high-T_c superconducting $Bi_2Sr_2CaCu_2O_{8+d}$ (Bi2212) were extensively studied [1]. Mesa-shaped Bi2212 THz sources are compact in size, has a broad tunability range, and extremely monochromic radiation. In many applications, polarization control of the THz radiation is required. However, commonly studied Bi2212 sources in the shape of a rectangular mesa are linearly polarized [2]. Circular polarization (CP) is achievable in Lab environments by using external optical devices such as quarter wave plates. Nevertheless, monolithic generation of CP is highly in demand for compact and portable devices.

In previous reports [3, 4], the CP THz emission from Bi2212 sources has been numerically studied. In the present study, we experimentally show a monolithic Bi2212 based source capable of generating CP THz radiation. The device discussed in this study is in the shape of a cylindrical mesa with two notches, one on each side of its diameter. In a temperature of 30 K, the polarization state, as represented by the axial ratio (AR), was found to be as low as 0.5 dB with a tunability between circular to elliptical polarization (> 3dB). The polarization properties are measured by using a rotating wire-grid polarizer in the emission path between the source and a Si-Bolometer.

References

[1] I. Kakeya and H. Wang, Supercond. Sci. Technol., vol. 29, no. 7, p. 73001, 2016.
[2] L. Ozyuzer, *et al*, Science, vol. 318, no. 5854, pp. 1291–1293, 2007.
[3] A. Elarabi, Phys. Procedia, vol. 81, pp. 133–136, 2016.
[4] H. Asai and S. Kawabata, Appl. Phys. Lett., vol. 110, 13261, 2017.

Keywords: Intrinsic Josephson Junctions, Terahertz, Polarization

F5

Investigations of the polarization behavior of high-T_c superconducting terahertz emitters.

Kyoto University[1], The University of Tsukuba[2], Argonne National Laboratory[3]

A. Elarabi[1,2], Y. Yoshioka[1], T. M. Benseman[3], G. Kuwano[2], M. Tsujimoto[2,3], T. Kashiwagi[2], K. Kadowaki[2], I. Kakeya[1].

High-T_c superconducting terahertz (THz) emitters has undergone a rapid and significant progress since its discovery [1]. Cutting-edge High-T_c Bi-2212 mesas can emit THz radiation with power as much as 110 μW [2], with wide frequency tunability range (0.5–2.4 THz) [3], and a relatively high temperature (77 K) [4]. Several studies have investigated the THz radiation properties from Bi-2212 mesas [5]. However, the polarization properties have yet to be experimentally studied [6,7]. Achieving polarization control using monolithic methods would eliminate the need for additional optical devices, which simplifies THz devices, increases its durability and reduces cost.

In this study, we present a comparative investigation of the polarization characteristics of THz radiation emitted from different types of mesa geometries. We demonstrate that by modifying the geometrical structure of the mesa, the polarization of the radiation can be monolithically controlled. Circular polarization (CP) with axial ratios (AR) as low as ~0.2 dB was achieved by using truncated edge square mesas at T_b = 21 K and side length l = 86 [8]. CP with AR = 0.5 dB was also achieved using notched cylindrical mesa with a radius of r_c = 40 μm at T_b = 30 K. Finally, linearly polarized emission with tunable major axis angle in the range of ~50° was measured at T_b = 72 K using rectangular mesa that has width of w = 60 μm, and length l = 310 μm. The polarization characteristics is experimentally presented and discussed. These findings expedite the development of new THz polarization synthesizers.

References:

[1] L. Ozyuzer, A. E. Koshelev, C. Kurter, et al., Science **318**, 1291 (2007).

[2] T. M. Benseman, K. E. Gray, A. E. Koshelev, et al., Appl. Phys. Lett. **103**, 22602 (2013).

[3] T. Kashiwagi, K. Sakamoto, H. Kubo, et al., Appl. Phys. Lett. **107**, 82601 (2015).

[4] H. Minami, C. Watanabe, T. Kashiwagi, et al., J. Phys. Condens. Matter **28**, 25701 (2016).

[5] I. Kakeya and H. Wang, Supercond. Sci. Technol. **29**, 73001 (2016).

[6] H. Asai and S. Kawabata, Appl. Phys. Lett. **110**, 132601 (2017).

[7] A. Elarabi, Y. Yoshioka, M. Tsujimoto, et al., Phys. Procedia **81**, 133 (2016).

[8] A. Elarabi, Y. Yoshioka, M. Tsujimoto, et al., arXiv:1711.01375 (2017).

Monolithic polarization control of THz radiation using Bi-2212 mesa geometrical structures.

Kyoto University [1], University of Tsukuba[2], °Asem Elarabi[1,2], Yusuke Yoshioka[1], Manabu Tsujimoto[2], Itsuhiro Kakeya[1]

E-mail: asemelarabi@sk.kuee.kyoto-u.ac.jp

In the past decade, continuous-wave terahertz sources made of high-Tc superconducting $Bi_2Sr_2CaCu_2O_{8+\delta}$ (Bi-2212) have been extensively studied [1]. Mesa-shaped Bi2212 terahertz sources are compact in size, have broad tunable frequency ranges, and monochromic radiations. In many applications, polarization controls of the terahertz radiation are needed. However, commonly studied Bi2212 sources in the shape of a rectangular mesa are linearly polarized [2]. Circular polarization (CP) is achievable in laboratory-environments by using external optical devices such as quarter-wave plates. Nevertheless, monolithic generation of CP is highly in demand for compact and portable devices.

Polarization control of THz emission from Bi-2212 has been numerically studies in multiple publications [3,4]. In the present study, we demonstrate experimentally, that the polarization can be monolithically controlled in Bi-2212 based sources by using the geometrical structure of the stacked Intrinsic Josephson junctions (IJJs) in a mesa form. The devices discussed here have mesas in the shape of a cylindrical structure with two notches on its sides (Fig. 1(b)), and a square with truncated edges (Fig. 1 (a)). Around 25 K, the polarization state, as represented by the axial ratio (AR), was found to be as low as 0.2 dB with a tunability between circular to elliptical polarization (AR > 3dB). The polarization properties are measured by using a rotating wire-grid polarizer in the emission path between the source and a Si-Bolometer.

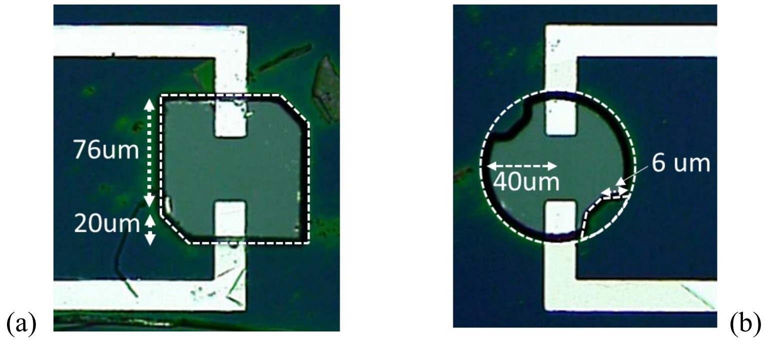

Fig. 1 (a) Truncated edge square mesa. (b) Cylindrical mesa with notched sides.

References:

[1] I. Kakeya and H. Wang, Supercond. Sci. Technol. **29**, 73001 (2016).

[2] L. Ozyuzer, et al, Science **318**, 1291 (2007).

[3] A. Elarabi, Y. Yoshioka, M. Tsujimoto, Y. Nakagawa, and I. Kakeya, Phys. Procedia **81**, 133 (2016).

[4] H. Asai and S. Kawabata, IEEE Trans. Appl. Supercond. **8223**, 1 (2016).

B-4

Bi2223 における固有ジョセフソン特性から見た CuO_2 多重層内部の不均一超伝導

京大院工 [A]、弘前大理工 [B]　掛谷一弘 [A]、野村義樹 [A]、岡本陸 [A]、足立伸太郎 [B]、渡辺孝夫 [B]

Inhomogeneous superconductivity inside the CuO_2 multiple layer probed by intrinsic tunneling spectroscopy in Bi2223

I. Kakeya[A], Y. Nomura[A], R. Okamoto[A], S. Adachi[B], and T. Watanabe[B]
Kyoto Univ. [A], *Hirosaki Univ.* [B]

超伝導についてもっとも多くの人が持つ疑問の一つは「超伝導転移温度T_cは何によって決められているのか？」という問であろう。銅酸化物高温超伝導体において既知となっている一つの答えとしては、「超伝導層を構成するCuO_2層の数nを増やせばT_cは上昇するが、$n = 3$を越えると減少する」という知識が挙げられる。我々はこの答えの中に、固有ジョセフソン接合（IJJ）を構成する多くの要素が含まれていることに気付くが、20年余り続いているIJJ特性に関する研究からは余り重要な情報が得られていない。これは、IJJの精密な解析に耐えうる良質の単結晶を$n = 3$の物質について育成することが困難であるために、系統的な実験結果が得られていないためである。FZ法により単結晶が得られる$Bi_2Sr_2Ca_2Cu_3O_{10+\delta}$ (Bi2223)の場合でも、$Bi_2Sr_2CaCu_2O_{8+\delta}$ (Bi2212) の層間析出が起きやすく、10%以下に抑えることは極めて困難である[1]。我々は、単結晶育成方法の改善により層間析出を抑えると同時に、少数層のIJJを取り出す微細加工技術を用いてBi2223だけからなるメサ構造IJJスタックを作成し、測定することに成功した[2]。本講演では、CuO_2三重層内部における不均一な超伝導分布に由来すると考察される、$n = 1,2$の物質とは本質的に異なる振る舞いについて報告する。

電流電圧特性に多重ブランチ構造が見られるBi2212メサ構造素子では、ゼロ抵抗の超伝導ブランチの最大電流が有限抵抗ブランチのそれらに比べて1/2以下となることが分かっている。このことは、最上部の超伝導層SL1に近接して蒸着されたAgにSL1の超伝導電子が浸みだした結果、SL1とSL2の秩序パラメータΨの重なりが減少するためと考えられている[3]。一方、Bi2223メサ構造において超伝導ブランチの最大電流の抑制はほとんど見られない。これは、SL1を構成する上部外側CuO_2面からの超伝導電子の浸み出しを内側CuO_2面が補償する結果、下部外側CuO_2面にはほとんど影響が出ていないためと考えられる。また、Bi2212では最大臨界電流密度J_cとT_cが1対1に対応していたが、Bi2223ではその限りではない。すなわち、J_cはOPのΨによって決定されるのに対して、T_cの決定にはIPの状態が無視できないということと理解される。また、固有トンネル分光の結果から、OPの超伝導ギャップや電子状態を議論する。

以上の考察は、IJJモデルではこれまで一様の超伝導電極と考えられていたSLが、CuO_2面にΨが局在しており、Bi2223では、IPが上下のOPを分離していると考慮する必要があることを示している。これは、Bi2223のスイッチング現象測定において、Bi2201, Bi2212では見られる隣接接合間の結合スイッチングが観測されないこととコンシステントである[4]。

[1] Y. Yamada, K. Anagawa, T. Shibauchi, T. Fujii, T. Watanabe, A. Matsuda, and M. Suzuki, Phys. Rev. B 68 054533 (2003).
[2] I. Kakeya, K. Hamada, T. Tachiki, T. Watanabe, and M. Suzuki, Supercond. Sci. Technol., 22, 114014 (2009).
[3] M. Suzuki, M. Ohmaki, R. Takemura, K. Hamada, T. Watanabe, K. Ota, H. Kitano, and A. Maeda, J. Phys.: Conf. Ser. 129, 012033 (2008).
[4] Y. Nomura, T. Mizuno, H. Kambara, Y. Nakagawa, I. Kakeya, and M. Suzuki, J. Phys. Conf. Ser. **507** (2014) 012038